NUMERICAL IMPLEMENTATION AND ANALYSIS OF A POROUS PLASTICITY MODEL FOR DUCTILE DAMAGE PREDICTION

A THESIS SUBMITTED TO
THE GRADUATE SCHOOL OF NATURAL AND APPLIED SCIENCES
OF
MIDDLE EAST TECHNICAL UNIVERSITY

BY

CAN ERDOĞAN

IN PARTIAL FULFILLMENT OF THE REQUIREMENTS
FOR
THE DEGREE OF MASTER OF SCIENCE
IN
AEROSPACE ENGINEERING

JANUARY 2021

Approval of the thesis:

NUMERICAL IMPLEMENTATION AND ANALYSIS OF A POROUS PLASTICITY MODEL FOR DUCTILE DAMAGE PREDICTION

submitted by **CAN ERDOĞAN** in partial fulfillment of the requirements for the degree of **Master of Science in Aerospace Engineering Department, Middle East Technical University** by,

Prof. Dr. Halil Kalıpçılar
Dean, Graduate School of **Natural and Applied Sciences** _____

Prof. Dr. İsmail Hakkı Tuncer
Head of Department, **Aerospace Engineering** _____

Assoc. Prof. Dr. Tuncay Yalçınkaya
Supervisor, **Aerospace Engineering, METU** _____

Examining Committee Members:

Prof. Dr. Altan Kayran
Aerospace Engineering, METU _____

Assoc. Prof. Dr. Tuncay Yalçınkaya
Aerospace Engineering, METU _____

Prof. Dr. Demirkan Çöker
Aerospace Engineering, METU _____

Assoc. Prof. Dr. Ercan Gürses
Aerospace Engineering, METU _____

Assoc. Prof. Dr. Cihan Tekoğlu
Mechanical Engineering, TOBB ETU _____

Date: 27.01.2021

I hereby declare that all information in this document has been obtained and presented in accordance with academic rules and ethical conduct. I also declare that, as required by these rules and conduct, I have fully cited and referenced all material and results that are not original to this work.

Name, Surname: Can Erdoğan

Signature :

ABSTRACT

NUMERICAL IMPLEMENTATION AND ANALYSIS OF A POROUS PLASTICITY MODEL FOR DUCTILE DAMAGE PREDICTION

Erdoğan, Can
M.S., Department of Aerospace Engineering
Supervisor: Assoc. Prof. Dr. Tuncay Yalçınkaya

January 2021, 82 pages

Ductile damage and fracture are known to be driven by the microvoid nucleation, growth, and coalescence. Porous micromechanical description of the ductile metals led to many phenomenological material models, which are used to predict the damage and fracture in engineering structures. In this thesis, the assessment of a rate-independent porous plasticity model is done through the representative volume element (RVE) calculations. The model is based on the formalism presented in [1] which is implemented as a user material subroutine through a prediction-correction scheme similar to a classical J2 plasticity framework. In this context, RVE's are taken from a periodic array of spherical voids surrounded by an elastoplastic matrix material with isotropic exponential hardening, and they are deformed under a constant triaxial stress state with a displacement controlled method. The implementation of the model and the method of the RVE calculations are explained in detail. Limitations of the original model are discussed, and a heuristics extensions to the constitutive framework is proposed to obtain a better fit between the porous model and the unit cell results in terms of volumetric void growth and equivalent stress-strain relation. Numerical analyses show the possibility of achieving a compact framework with a straightfor-

ward implementation that agrees well with the RVE simulations for a wide range of stress triaxiality values. The present framework is compared with the widely used Gurson-Tvergaard-Needleman (GTN) model and the differences are discussed. A simple void coalescence relation is added to this framework to simulate the final failure phase of ductile deformation. Additionally, tension simulations with smooth and blunt notched specimens are performed with the GTN model, the present porous plasticity model, and the Johnson-Cook uncoupled damage model to address the model's performance in a ductile fracture simulation. Results show that the present framework and the GTN model can yield almost identical results in notched simulations in terms of engineering stress-strain response and the porosity evolution. The thesis is concluded with an outlook and possible future improvements.

Keywords: Porous Plasticity, Representative Volume Element, Ductile Damage, Fracture

ÖZ

SÜNEK HASAR TAHMİNİ İÇİN GÖZENEKLİ BİR PLASTİSİTE MODELİNİN SAYISAL UYGULAMASI VE ANALİZİ

Erdoğan, Can
Yüksek Lisans, Havacılık ve Uzay Mühendisliği Bölümü
Tez Yöneticisi: Doç. Dr. Tuncay Yalçınkaya

Ocak 2021 , 82 sayfa

Sünek hasar ve kırılmanın mikro boşluk oluşumu, büyümesi ve birleşmesinden kaynaklandığı bilinmektedir. Sünek metallerin gözenekli mikromekanik tanımı, mühendislik malzemelerinde hasar ve kırılmayı tahmin etmek için kullanılan birçok fenomenolojik malzeme modeline yol açmıştır. Bu tezde, hızdan bağımsız bir porlu plastisite modelinin değerlendirmesi, temsili hacim elemanı (THE) hesaplamaları aracılığıyla yapılmıştır. Model, [1]'de sunulan formulasyona dayanmaktadır ve klasik bir J2 plastisite uygulamasına benzer bir deneme-düzeltme şeması aracılığıyla kullanıcı malzeme altprogramı olarak uygulanmıştır. Bu bağlamda, THE'ler izotropik üstel sertleşmeye sahip elastoplastik bir matris malzemesi ile çevrili periyodik küresel boşluk dizisinden alınmış ve yer değiştirme kontrollü bir yöntemle sabit üç eksenli gerilim altında deforme edilmişlerdir. Modelin uygulanması ve RVE hesaplamalarının yöntemi ayrıntılı olarak açıklanmıştır. Orijinal modelin sınırlamaları tartışılmıştır. Hacimsel boşluk büyümesi ve eşdeğer gerilim-gerinim ilişkisi açısından model ile THE sonuçları arasında daha iyi bir uyum elde etmek için modele bir modifikasyon önerilmiştir. Sayısal analizler, bütün üç eksenli gerilim değerleri için THE simülasyonları

ile uyum gösterebilen ve uygulaması basit olan kompakt bir modelin elde edilebileceğini göstermiştir. Yaygın olarak kullanılan Gurson-Tvergaard-Needlman (GTN) modeli ve mevcut model ile karşılaştırmalar yapılmıştır ve farklılıklar tartışılmıştır. Sünek malzemelerde son kırılma aşamasını simüle etmek için bu modele basit bir boşluk birleştime ilişkisi katılmıştır. Ek olarak, sünek kırılma simülasyonlarnda modelin performansını ele almak için GTN modeli, mevcut gözenekli plastisite modeli ve Johnson-Cook ayrık hasar modeli ile düz ve keskin olmayan çentikli çekme numuneleri ile kırılma simülasyonları gerçekleştirilmiştir. Sonuçlar, mevcut modelin ve GTN modelinin çentikli numunelerde mühendislik gerilim-gerinim ilişkisi ve porozite değişimi açısından neredeyse aynı sonuçları verebildiği gösterilmiştir. Tez, genel bir bakış açısı ve gelecekteki olası iyileştirmelerle sonuçlandırılmıştır.

Anahtar Kelimeler: Porlu Plastisite, Temsili Hacim Elemanı, Sünek Hasar, Kırılma

To my family...

ACKNOWLEDGMENTS

First and foremost, I would like to deeply thank my supervisor, Assoc. Prof. Dr. Tuncay Yalçınkaya, for his exceptional guidance and support throughout my education. His motivation and dedication to research have been an inspiration to me.

I am highly grateful to Prof. Dr. Alan Cocks and Assoc. Prof. Dr. Cihan Tekoğlu for their insightful discussions and input on the work.

I wish to thank Izzet Tarık Tandoğan and other members of the research group of Dr. Yalçınkaya for their contributions. Also, I would like to thank Dilek Güzel for her friendship.

I owe a special thanks to Gül Demirer who has always been there for me, encourage and support me.

Most importantly, I am sincerely grateful to my parents, Hatice Erdoğan and Yılmaz Erdoğan, and to my brother Kaan Erdoğan for their endless love and support.

I gratefully acknowledge the support of the Scientific and Technological Research Council of Turkey (TUBİTAK) under the 3501 program (Grant No. 117M106).

TABLE OF CONTENTS

LIST OF TABLES

TABLES

LIST OF FIGURES

FIGURES

LIST OF ALGORITHMS

ALGORITHMS

CHAPTER 1

INTRODUCTION

One of the most critical concepts in material science and engineering is the fracture phenomenon. There are mainly two possible modes of fracture in engineering materials, namely ductile and brittle. The difference between these two mechanisms is the amount of plastic deformation before the fracture. Brittle fracture occurs with minimal plastic deformation, and small cracks can quickly lead to complete failure of the material, which is an undesirable property for an engineering material. A small plastic zone develops ahead of the crack tip, and the phenomenon is called small scale yielding. On the other hand, ductile materials show large plastic deformations before separation with more stable and predictable crack propagation. The plasticity does not occur only ahead of the crack tip. It rather spreads largely in the specimen. Therefore it is referred to as large scale yielding. Ductile fracture is known to be the most commonly observed fracture mode in engineering metals at room temperature; thus, it is essential to understand the fundamental mechanisms especially for manufacturing and metal forming applications where excessive plastic deformations are present. The ductile fracture mode is known to be driven by the microvoid nucleation, growth and coalescence. With the early observations on the porous mechanism of ductile fracture [2] and computational works [3, 4], a serious amount of research is focused on the area for more than 50 years in terms of both micromechanical examinations through experimental and computational studies and predictive modeling techniques. The micromechanical phenomena behind the ductile fracture are explained briefly in the following section.

1.1 Micromechanical aspects

The void nucleation phase is linked to the second phase particles, or inclusions [5]. Microvoids or pores nucleate at the boundary of a second phase particle or an inclusion and matrix material. Alternatively, voids formation can occur by internal cracking of the hard second phase particles (see Figure 1.1). Nucleation by debonding is usually the mechanism with the soft matrix materials, and nucleation mode changes to particle cracking as the matrix material gets harder (see [6]). The mode of nucleation depends on factors such as the hardening behavior of the matrix, the inclusion or particle geometry, and the stress state (see e.g. [7–9]). Although it is intuitive to assume that the voids nucleate under tensile loads, it is shown that shear can also cause void formation by debonding of the particle and the matrix interface (see [10]). It should be noted that the void nucleation cannot be captured macroscopically because the size of the second phase particle or inclusion is relatively small to bring any significant porosity.

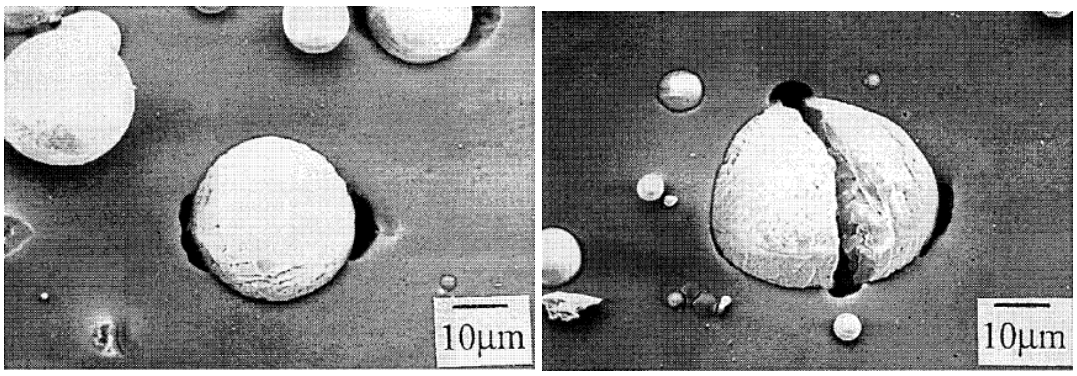

(a) (b)

Figure 1.1: Different mechanism of void nucleation. (a) Decohesion of the particle-matrix interface, (b) particle cracking, from [11].

The ductile damage initiates with the void nucleation and continues with void growth. Microvoid growth is driven by the plastic deformation of the surrounding matrix. The growth is studied on artificially inserted holes under tension in [12] (see Figure 1.2). Voids first elongate vertically in the loading direction. Then, the deformation mode changes due to necking induced increase in the stress triaxiality around the voided

region, and voids start to extend horizontally. The prominent effect of stress triaxiality on the void growth is reported in literature (see e.g. [13–18]). A substantial increase in void growth is observed with increasing stress triaxiality. Consequently, the fracture strain decreases dramatically as shown by Cox and Law [19] through tensile tests of notched specimens. Stress triaxiality is the ratio of the hydrostatic stress to the von Mises equivalent stress formulated as

$$T = \frac{\sigma_h}{\sigma_{eq}}, \tag{1.1}$$

and it is considered to be the primary factor in the evolution of ductile damage through the void growth mechanism.

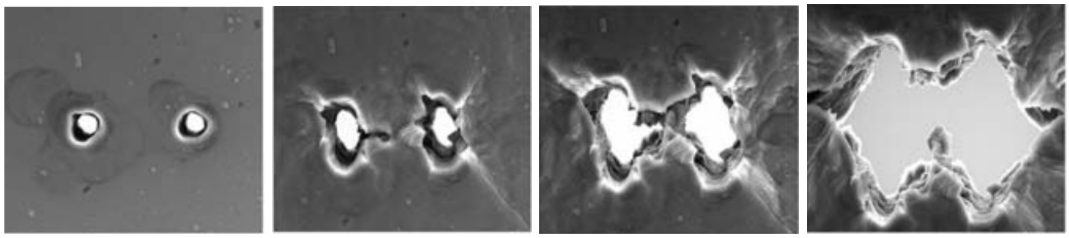

(a) (b) (c) (d)

Figure 1.2: The growth and the coalescence of artificially inserted voids in a sheet metal, from [12].

Although the effect of stress triaxiality is clear, it was shown that the Lode parameter, which is related to the third invariant of stress, also has a notable effect on ductility [20]. Experiments on double notched tube specimens under combined tension and shear indicate that ductility drops under shear dominated loads ($L \approx 0$). Lode parameter is defined as

$$L = \frac{2\sigma_{II} - \sigma_I - \sigma_{III}}{\sigma_I - \sigma_{III}} \tag{1.2}$$

where σ_I, σ_{II} and σ_{III} are the principal stress components with $\sigma_I \geq \sigma_{II} \geq \sigma_{III}$.

The final stage of the fracture process in ductile materials is void coalescence. Coalescence is considered to cause failure in two distinct mechanisms according to Tekoğlu et al. [21]. First mode occurs after significant void growth taken over by the plastic flow localization between adjacent voids that cause internal necking (see Figures 1.2c, 1.2d, 1.3a, from [12, 19]). The second one is by internal shearing of the ligament

between voids (see Figure 1.3b, from [19]). Shear can link two distant voids, which causes a shear band to occur. The deformation localizes, and fracture proceeds in this so-called thin void sheet. Eventually, microcracks initiate from the void coalescence sites, and with further straining of the material, crack propagation causes fracture.

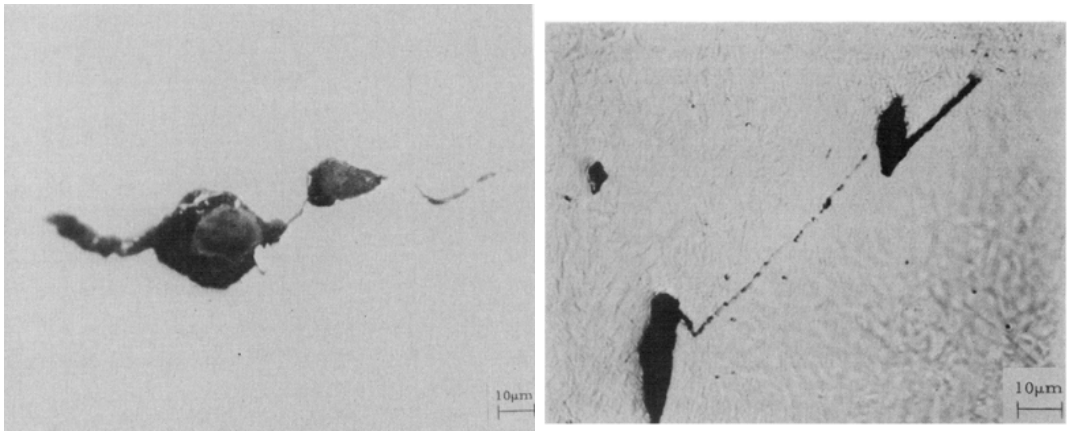

(a) (b)

Figure 1.3: Mechanisms of void coalescence. (a) Internal necking, (b) internal shearing, from [19].

1.2 Modelling of ductile damage and failure

The porosity based micromechanical description of the ductile failure in metallic alloys led to many different modeling approaches in the literature. The focus will be on the Continuum Damage Models (CDM) in the current work. In CDM, instead of incorporating the micromechanical properties directly into the simulation, they are phenomenologically presented by internal parameters in the constitutive equations. The most basic models include a stress reduction factor based on a single damage parameter, D, as $\sigma = (1 - D)\sigma$, first introduced in [22]. Empirical relations are usually preferred for the evolution of D based on experimental studies or analytical derivations (see e.g. [23, 24]). These models where the stress is directly affected by the damage parameters are known as coupled models. Another approach to the ductile fracture modeling is based on the uncoupled models, where the damage induced material degradation is disregarded until the onset of failure of the structure. The ad-

vantage is that the implementation of such models is relatively easy, and the computational cost is reduced compared to the coupled models while having similar prediction capabilities. The uncoupled approach usually utilizes a surface-based prediction where the fracture surface is defined by D, and the evolution of D is based on strain and stress state. One example of the fracture surface models is the Johnson-Cook (JC) model [25] where the damage predictions are made in terms of stress triaxiality, strain rate and temperature. Some recent models are the modified Mohr-Coulomb model (MMC), which has been extensively used in rock and soil mechanics and extended to ductile fracture in [26], and Hasford-Coulomb (HC) model [27], which is an extension of the MMC model. The MMC and HC and other models in [28, 29] use a definition based on stress triaxiality and Lode parameter to predict a fracture surface.

The first studies on the continuum modeling of ductile damage and fracture directly derived from porous bodies are conducted by McClintock [3] and Rice and Tracey [4] using cylindrical and spherical isolated voids in a rigid-perfectly plastic infinite matrix material. The Rice and Tracey model was later extended by Huang [30] for the dilatation rates at different stress triaxiality regions. Also, an uncoupled model is derived from the Rice and Tracey model in [13]. Another coupled model is proposed by Rousselier [31] based on the continuum damage mechanics and thermodynamics following the work of Lemaitre [32]. An extension is proposed to the Rousselier model based on the unit cell simulations in [33]. Although coupled models are computationally more intensive, they provide a more realistic description of the damage evolution, and they also account for the degradation of stress carrying capacity, which results in strain localization leading to the final failure.

Another phenomenological ductile damage model was introduced by Gurson [34] using upper-bound limit load analysis for the deformation of spherical and cylindrical voids in a plastic matrix. The Gurson model uses only the void volume fraction, f, as the damage variable. The evolution of f is governed by the incompressibility of the plastic matrix material as, $\dot{f} = (1-f)tr(\dot{\boldsymbol{\varepsilon}}^p)$. The model also utilizes a correction for the hardening of the material since a voided body does not strain harden as a homogeneous one. Correction is done through a plastic work equality given by $(1-f)\bar{\sigma}\dot{\bar{\varepsilon}} = \boldsymbol{\Sigma} : \dot{\boldsymbol{E}}$, where the $\bar{\sigma}$ & $\bar{\varepsilon}$ are the equivalent stress and strain of

the microscopic voided body and $\boldsymbol{\Sigma}$ & $\boldsymbol{E}$ are related to the macroscopic response. Additionally, the plastic flow is found from the associative flow rule in the Gurson model. It should be noted that the original model can only predict the growth of existing pores and disregards the nucleation of new voids. Void nucleation criterion is added to the Gurson model in [35] using a statistical approach. Recently nucleated voids simply added to the currently growing voids with $f = f_G + f_N$. The yield potential of Gurson model is extended based on a bifurcation study by Tvergaard [36, 37]. Extension is done using q_1 and q_2 parameters and the modified potential is given in the following equation

$$\phi = \frac{\sigma_{eq}}{\sigma_y} + 2q_1 f cosh(\frac{3q_2\sigma_m}{2\sigma_y}) - (1 + q_1^2 f^2). \tag{1.3}$$

Although these parameters are initially used to account for void interaction effects, studies have shown that they are not universal and they depend on the loading conditions and geometry (see [38–40]). Consequently, they are mostly used to fit the Gurson model for different materials and loading states. Void coalescence relation is introduced in [41] to simulate the rapid loss of stress carrying capacity at the final failure phase of the deformation. The coalescence model uses an effective porosity relation shown in the following equation

$$f^\star = \begin{cases} f & \text{if } f \leq f_c \\ f_c + \kappa(f - f_c) & \text{if } f > f_c. \end{cases} \tag{1.4}$$

Porosity, f, is replaced by the effective porosity, $f^\star$, in the yield potential which artificially increases the porosity after a critical value and accelerates the void growth. In Eq. (1.4), f_c is the critical porosity and κ determines the acceleration level of the void growth. With the initial model of Gurson and improvements of Tvergaard and Needleman, this formulation is called the GTN model which has been one of the most referenced computational porous plasticity models.

Several extensions for the GTN model have been proposed. Void shape effects are incorporated in the Gologanu-Leblond-Devaux (GLD) model [42–44]. Effect of the Lode parameter is added in terms of an additional void evolution term based on shear loads in [45–47]. The performance of the shear modified Gurson model is addressed in [48,49]. The former uses unit cell analysis, while the latter makes comparisons with experiments and also compares with the uncoupled MMC fracture model. Moreover,

plastic anisotropy [50], void size effects [51–53] and recently hydrogen microvoid interaction [54] are included in a GTN type framework. Although more advanced forms of the GTN model have been suggested, the original form of the model is still being used to anticipate damage and fracture in ductile metals (see [55]).

Similar to the analysis of Gurson, an alternative yield potential for a porous plastic body is proposed by Cocks [1] using a lower-bound limit analysis for the growth of a spherical void. The priority of the regarding model was simplicity; thus, the present constitutive framework is more straightforward and compact compared to the models mentioned previously. The model has the porosity, f, as the only damage variable. The yield potential utilizes an effective stress expression, which includes both von Mises equivalent and hydrostatic stress along with two functions of void volume fraction, f, affecting the two parts of the stress state separately. The model's effective stress is only a function of stress and porosity and does not depend on yield stress, which is a fundamental difference from the Gurson model. Subsequent works in [56–60] use similar potentials for porous bodies but only for the viscoplastic materials. Cocks initially proposed formulations for both rate-independent and creeping porous materials; however, such models are used solely for the prediction of creep phenomenon or to analyze the densification of metal powders. Both of these applications include a rate-dependent formulation. One of the primary focuses of the current thesis is to utilize the rate-independent yield potential for the ductile damage prediction which has not been addressed in the literature.

It is necessary to mention the representative volume element (RVE) analysis for the predictive modeling of ductile damage and fracture. An RVE can be considered as a small finite portion of a material that carries the micromechanical properties. In the context of porous materials, the real material with different grain orientations, second phase particles, and random distribution of voids is idealized as a homogeneous elastoplastic material with a periodic distribution of voids. RVE's are taken from an idealized material, as shown in Figure 1.4, and they are usually deformed under constant stress triaxiality and Lode parameter. This approach, first introduced by Needleman [61], has been a convenient numerical tool to investigate void evolution in terms of shape and volume, void coalescence, and subsequent material degradation. RVE's are mainly adopted to gather information about the micromechanics of voids

and the results are used for the evaluation and calibration of continuum damage and fracture models. The pioneering work by Koplik and Needleman [38] is conducted through axisymmetric voided RVE models, and the results are used to identify the fitting parameters of the GTN model. Different aspects of the micro-void growth and coalescence mechanisms are studied extensively in the literature. Similar to the work of Koplik and Needleman, the combined effect of initial porosity and stress triaxiality is studied in [62]. The effect of initial void shape is studied by Pardoen and Hutchinson [63] using initially non-spherical voided axisymmetric RVE's under constant triaxiality. They proposed a coalescence model considering the void shape. The effect of Lode parameter is studied in [64,65] utilizing 3D RVE models under constant T and L. Studies indicate that as the load gets shear dominant, ductility decreases, and the fracture mode changes from internal necking to internal shearing. Additionally, crystal plasticity based analysis is conducted on such RVE models in [66–68] to examine the effect of grain orientation on void shape and growth.

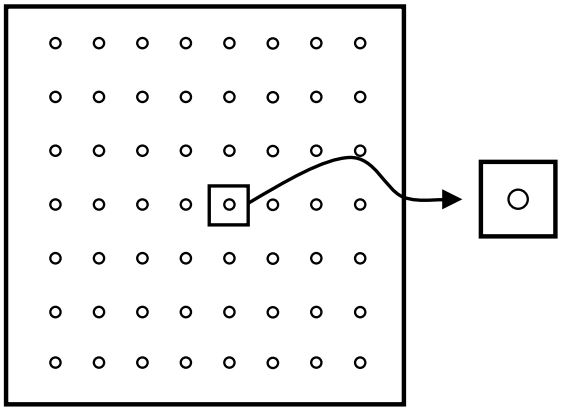

Figure 1.4: Idealized system of periodic void distribution and an RVE element in 2D.

Moreover, void nucleation has been studied through RVE analysis by replacing the void with an inclusion or second phase particle. Works in [69, 70] examined the local stress and strain with the assumption of perfect bonding between the matrix and the inclusion. Another approach is using the cohesive zone elements to simulate the separation of particle and the matrix (see [71]). Cohesive elements are placed between the inclusion and the matrix in finite element (FE) model, and the nucleation is simulated with the separation of the cohesive element. Shabrov and Needleman [72]

extended the cohesive zone approach and studied the effects of multiple inclusions and inclusion distribution in the matrix.

Although there have been numerous studies on the poro-mechanical damage and fracture models, they have mostly focused on frameworks based on the Gurson model. The advanced models, such as the GLD model [44] or the shear modified Gurson model [46], have been proven to improve the existing frameworks, which brings complexity and additional parameters to deal with. Such models are highly capable for the analysis of micro-void mechanisms. However due to the complicated formulations of such models, their usage is limited in engineering applications. The current thesis aims to provide a simple constitutive framework and implementation scheme for an alternative porous plasticity formulation based on the yield potential of Cocks [1]. The implementation is done following a basic predictor-corrector scheme with a numerical calculation of consistent tangent modulus. The model is assessed in the context of rate-independent ductile damage and fracture through RVE simulations performed on 3D finite element models. An extension is proposed for the framework based on the RVE results and the model's predictions. The performance of the model is addressed using tension simulations on smooth and notched bars, and comparisons are made with the well-known GTN model and the Johnson-Cook uncoupled fracture model.

The organization of the theses is as follows. In Chapter 2, the formulation is shown and the implementation is discussed in detail. The RVE study is explained in Chapter 3, and in Chapter 4, the results are presented and discussed for both the RVE study and the porous plasticity model together with the tension simulations. The thesis is concluded with an outlook and future remarks in Chapter 5.

CHAPTER 2

FORMULATION AND IMPLEMENTATION OF THE POROUS PLASTICITY MODEL

2.1 Formulation of the model

The constitutive formulation of the rate-independent porous plasticity model is presented in this section. The model employs the below presented form of the yield potential initially proposed in [1] which includes effective stress, $\bar{\sigma}$, and yield stress, σ_y. The potential is obtained based on the limit analysis of a plastic body containing a hexagonal periodic array of spherical voids. The representation of the yield potential is similar to a classical von Mises plasticity model with an additional dependence on the mean stress and two porosity functions g_1 and g_2. Effective stress is only a function of local stress, $\boldsymbol{\sigma}$, and porosity, f; thus, yield stress can be treated separately in this model, which is a condition that is not observed in the Gurson type models:

$$\phi = \bar{\sigma} - \sigma_y = \sqrt{\frac{\sigma_{eq}^2}{g_1(f)} + \frac{\sigma_m^2}{g_2(f)}} - \sigma_y \tag{2.1}$$

where g_1 and g_2 are the functions of void volume fraction f, σ_{eq} is the von Mises stress, σ_m is the hydrostatic or mean stress and they can be defined as

$$\sigma_{eq} = \sqrt{\frac{3}{2} dev(\boldsymbol{\sigma}) : dev(\boldsymbol{\sigma})}, \;\; \sigma_m = \frac{1}{3}(tr(\boldsymbol{\sigma})). \tag{2.2}$$

In Eq. (2.2), $tr(\boldsymbol{\sigma})$ is the trace of the stress tensor ($tr(\boldsymbol{\sigma}) = \sigma_{ii} = \sigma_{11} + \sigma_{22} + \sigma_{33}$), $dev(\boldsymbol{\sigma})$ is the deviatoric part of the stress tensor ($dev(\sigma_{ij}) = \sigma_{ij} - \frac{1}{3}\,\sigma_{kk}\,\delta_{ij}$) and ':' is the double contraction operator. In the present thesis, bold symbols are used to represent second order tensors (e.g. $\boldsymbol{\sigma}$, $\boldsymbol{\varepsilon}$).

The porosity functions proposed in [1] are

$$g_1(f) = \frac{(1-f)^2}{1+\frac{2}{3}f}, \quad g_2(f) = \frac{2}{9}\frac{(1+f)(1-f)^2}{f}. \tag{2.3}$$

The behavior of porosity functions is illustrated in Figure 2.1 together with the shape of yield surface in terms of equivalent and the mean stress, which shows a hydrostatic stress dependent yield behavior. Note that with the given g functions, the model recovers the original von Mises plasticity at zero porosity.

The initial proposition of the model uses the basic kinematic void growth relation, as

$$\dot{f} = \frac{d}{dt}\left(\frac{V_f}{V}\right) \tag{2.4}$$

where V_f is the volume of voids and V is the total volume of the body. Since the matrix around the void is assumed to be incompressible, it can be concluded that the volume change in a body can only originate from the volume of voids; hence, $\dot{V}_f = \dot{V}$. Then, the evolution of porosity can be found as follows:

$$\dot{f} = \frac{d}{dt}\left(\frac{V_f}{V}\right) = \frac{\dot{V}_f V - \dot{V} V_f}{V^2} = \left(\frac{V-V_f}{V}\right)\frac{\dot{V}_f}{V} = \left(1-\frac{V_f}{V}\right)\frac{\dot{V}}{V}. \tag{2.5}$$

Since $V_f/V = f$ and $\dot{V}/V$ can be defined as $\dot{\boldsymbol{\varepsilon}}_v (= \dot{\boldsymbol{\varepsilon}}_{ii})$ with the small strain assumption, then Eq. (2.5) can be stated as,

$$\dot{f} = (1-f)tr(\dot{\boldsymbol{\varepsilon}}^p) = (1-f)\dot{\boldsymbol{\varepsilon}}^p_v. \tag{2.6}$$

Here, it is also assumed that the elastic deformations have a negligible effect on void growth. It should be noted that, the current formulation can only predict the growth of existing voids and does not include void nucleation.

Plastic part of the strain is calculated from the associative flow rule, as

$$\dot{\boldsymbol{\varepsilon}}^p = \dot{\gamma}\,\frac{\partial \phi}{\partial \boldsymbol{\sigma}} \tag{2.7}$$

where γ is the flow multiplier, and the direction of the plastic flow increment is assumed to be $\partial\phi/\partial\boldsymbol{\sigma}$, which also means that the plastic flow is in the normal direction to the yield surface. Due to the mean stress dependence on yield function, Eq. (2.7) can also provide hydrostatic part of the plastic strains which is required for the porosity evolution.

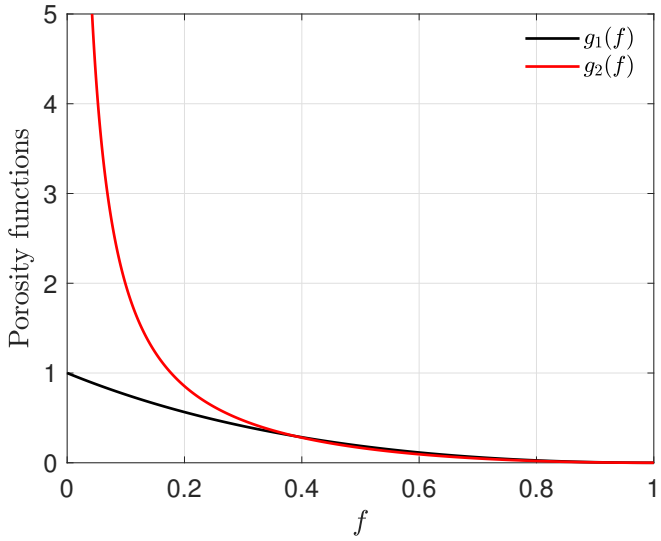

(a)

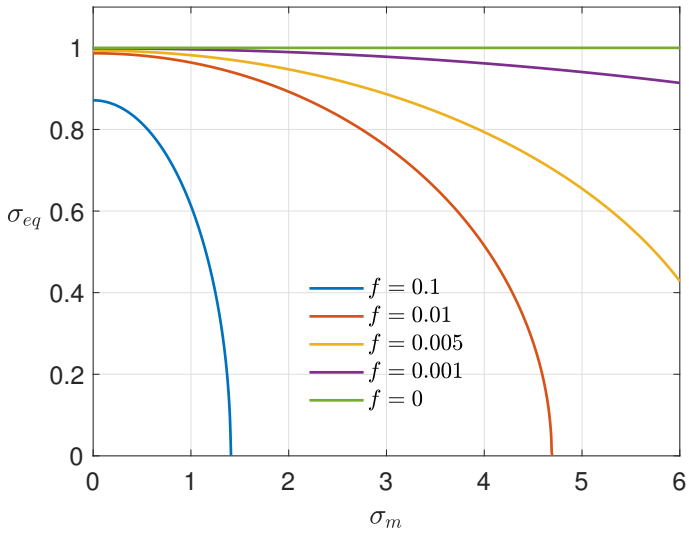

(b)

Figure 2.1: (a) Evolution of the porosity functions vs f, (b) yield surface representation of the porous plasticity model at different porosity levels.

Preliminary results using the model has recently been presented at a conference proceeding [73] using slightly different porosity functions in the yield potential. Although the model can anticipate the void growth and equivalent stress-strain relation at moderate to low stress triaxiality, it had certain issues at high stress triaxiality

regimes. The performance of the model was also demonstrated by a necking simulation. It should be noted that it is possible to get similar results with the porosity functions in [73] and the original suggestions of Cocks in [1]; however, the g functions of Cocks are used in the current study in order not to add extra variables.

2.2 Numerical implementation

In this section, numerical implementation of the porous plasticity model is demonstrated in detail. Solution of the nonlinear constitutive equations requires a local numerical integration scheme within the global finite element algorithm. The local integration is performed in the material subroutine (UMAT, [74]) in commercial finite element program Abaqus employing the classical radial return algorithm with elastic predictor and plastic corrector steps. In the UMAT subroutine, Abaqus provides the total strain for the current increment and expects users to calculate the stress and the consistent tangent modulus. The numerical implementation of the model covers the procedure to compute the stress and consistent tangent modulus using the constitutive formulations of the porous plasticity model along with the incremental update of the state variables.

Procedure for the present model follows the basic von-Mises (J2) plasticity framework. The conditions can be stated as follow:

1. The material is linear elastic before the yield point. In the elastic regime, stress is governed by the Hooke's law. Elastic region is restricted by the yield surface, ϕ.

2. The evolution of the yield surface is governed by both the yield stress (σ_y) and the porosity (f). Note that $0 \leq f \leq 1$.

3. Loading/Unloading conditions: If the loading is elastic, $\phi < 0$, then no plastic flow occurs, $\dot{\gamma} = 0$ & $\dot{f} = 0$. If the material deforms plastically, $\phi = 0$, then $\dot{\gamma} > 0$ & $\dot{f} \neq 0$, and the stress cannot go beyond the yield surface, $\phi \leq 0$.

4. Strain is decomposed additively into elastic and plastic parts, $\boldsymbol{\varepsilon} = \boldsymbol{\varepsilon}^e + \boldsymbol{\varepsilon}^p$.

Note that, the tensorial variables are stored as matrices in the Voigt notation in UMAT subroutine. Therefore, stresses and strains are as 6x1 vectors and tangent modulus, $\mathbb{C}$, is a 6x6 matrix as

$$\boldsymbol{\sigma} = \begin{bmatrix} \sigma_{11} \\ \sigma_{22} \\ \sigma_{33} \\ \sigma_{12} \\ \sigma_{13} \\ \sigma_{23} \end{bmatrix}, \boldsymbol{\varepsilon} = \begin{bmatrix} \varepsilon_{11} \\ \varepsilon_{22} \\ \varepsilon_{33} \\ \gamma_{12} \\ \gamma_{13} \\ \gamma_{23} \end{bmatrix}, \mathbb{C} = \begin{bmatrix} \mathbb{C}_{1111} & \mathbb{C}_{1122} & \mathbb{C}_{1133} & \mathbb{C}_{1112} & \mathbb{C}_{1113} & \mathbb{C}_{1123} \\ \mathbb{C}_{2211} & \mathbb{C}_{2222} & \mathbb{C}_{2233} & \mathbb{C}_{2212} & \mathbb{C}_{2213} & \mathbb{C}_{2223} \\ \mathbb{C}_{3311} & \mathbb{C}_{3322} & \mathbb{C}_{3333} & \mathbb{C}_{3312} & \mathbb{C}_{3313} & \mathbb{C}_{3323} \\ \mathbb{C}_{1211} & \mathbb{C}_{1222} & \mathbb{C}_{1233} & \mathbb{C}_{1212} & \mathbb{C}_{1213} & \mathbb{C}_{1223} \\ \mathbb{C}_{1311} & \mathbb{C}_{1322} & \mathbb{C}_{1333} & \mathbb{C}_{1312} & \mathbb{C}_{1313} & \mathbb{C}_{1323} \\ \mathbb{C}_{2311} & \mathbb{C}_{2322} & \mathbb{C}_{2333} & \mathbb{C}_{2312} & \mathbb{C}_{2313} & \mathbb{C}_{2323} \end{bmatrix}. \tag{2.8}$$

Here, notice also that shear strains are stored as engineering strains $\gamma_{ij} = 2\varepsilon_{ij}$ for $i \neq j$. The implementation of the numerical model should be done considering these conventions. Moreover, the total strain tensor in current increment is rotated to account for rigid body rotation before Abaqus calls UMAT subroutine for finite strain problems; thus, the user defined tensorial variables, such as plastic strains, have to be rotated at the start of the subroutine to assure that all of the direction dependent variables have the same orientation. Abaqus provides the relevant rotation operator for the UMAT under the name of ROTSIG.

The Cauchy or true stress is used as the stress measure in a UMAT subroutine which can be written as

$$\boldsymbol{\sigma} = \kappa\, tr(\boldsymbol{\varepsilon}^e)\mathbf{1} + 2\mu\, dev(\boldsymbol{\varepsilon}^e) \tag{2.9}$$

where κ is Bulk Modulus, μ is Shear Modulus, $dev(\boldsymbol{\varepsilon}^e)$ is the deviatoric part of the elastic strain tensor ($dev(\boldsymbol{\varepsilon}^e) = \boldsymbol{\varepsilon}^e - \frac{1}{3}\, tr(\boldsymbol{\varepsilon}^e)\, \mathbf{1}$), $tr(\boldsymbol{\varepsilon}^e)$ is the trace of elastic strain tensor ($tr(\boldsymbol{\varepsilon}^e) = \varepsilon^e_{11} + \varepsilon^e_{22} + \varepsilon^e_{33}$) and $\mathbf{1}$ is the second order identity tensor.

As stated previously, in a finite element simulation, total strain tensor $\boldsymbol{\varepsilon}$ is passed in the UMAT subrotuine for the calculation of the stresses from the constitutive model at each integration point. To be able to compute the stresses from Eq. (2.9), elastic and plastic parts of the total strain tensor have to be determined.

Elastic and plastic parts of the strain tensor can further be divided into deviatoric and hydrostatic components as

$$\begin{aligned} \boldsymbol{\varepsilon}^e &= tr(\boldsymbol{\varepsilon}^e)\mathbf{1} + dev(\boldsymbol{\varepsilon}^e), \\ \boldsymbol{\varepsilon}^p &= tr(\boldsymbol{\varepsilon}^p)\mathbf{1} + dev(\boldsymbol{\varepsilon}^p). \end{aligned} \tag{2.10}$$

Therefore, the Cauchy stress can be written as follows

$$\boldsymbol{\sigma} = \kappa\,(tr(\boldsymbol{\varepsilon}) - tr(\boldsymbol{\varepsilon}^p))\mathbf{1} + 2\mu\,(dev(\boldsymbol{\varepsilon}) - dev(\boldsymbol{\varepsilon}^p)). \tag{2.11}$$

Plastic part of the strain tensor is governed by the associative plastic flow rule:

$$\dot{\boldsymbol{\varepsilon}^p} = \dot{\gamma}\,\frac{\partial \phi}{\partial \boldsymbol{\sigma}} = \dot{\gamma}\,\left(\frac{3}{2}\frac{dev(\boldsymbol{\sigma})}{\bar{\sigma} g_1} + \frac{1}{9}\frac{tr(\boldsymbol{\sigma})}{\bar{\sigma} g_2}\mathbf{1}\right), \tag{2.12}$$

where γ is the plastic multiplier that determines the amount of plastic strain, ϕ is the yield potential, $\partial\phi/\partial\boldsymbol{\sigma}$ determines the direction of the plastic flow, and the $\bar{\sigma}$ is the effective stress as

$$\bar{\sigma} = \sqrt{\frac{3}{2}\frac{dev(\boldsymbol{\sigma}) : dev(\boldsymbol{\sigma})}{g_1(f)} + \frac{1}{9}\frac{(tr(\boldsymbol{\sigma}))^2}{g_2(f)}}. \tag{2.13}$$

Constitutive equations are then integrated using backward Euler scheme, which can be summarized for two arbitrary variables a and b, as

$$\dot{a} = b \rightarrow \frac{a_{n+1} - a_n}{\Delta t} = b_{n+1}. \tag{2.14}$$

Then the numerical integration of the equations are as follows:

$$\boldsymbol{\varepsilon}^p_{n+1} = \boldsymbol{\varepsilon}^p_n + \Delta\gamma\left(\frac{3}{2}\frac{dev(\boldsymbol{\sigma}_{n+1})}{\bar{\sigma}_{n+1}\, g_{1,n}} + \frac{1}{9}\frac{tr(\boldsymbol{\sigma}_{n+1})}{\bar{\sigma}_{n+1}\, g_{2,n}}\mathbf{1}\right), \tag{2.15}$$

$$\bar{\varepsilon}^p_{n+1} = \bar{\varepsilon}^p_n + \Delta\gamma, \tag{2.16}$$

$$f_{n+1} = \frac{f_n + tr(\boldsymbol{\varepsilon}^p_{n+1}) - tr(\boldsymbol{\varepsilon}^p_n)}{1 + tr(\boldsymbol{\varepsilon}^p_{n+1}) - tr(\boldsymbol{\varepsilon}^p_n)} = \frac{f_n + \Delta\gamma\left(\frac{1}{3}\frac{tr(\boldsymbol{\sigma}_{n+1})}{\bar{\sigma}_{n+1}\, g_{2,n}}\right)}{1 + \Delta\gamma\left(\frac{1}{3}\frac{tr(\boldsymbol{\sigma}_{n+1})}{\bar{\sigma}_{n+1}\, g_{2,n}}\right)}, \tag{2.17}$$

where n and $n+1$ subscripts denote the previous and current increments, respectively, and $\bar{\varepsilon}^p$ is the accumulated (equivalent) plastic strain. Here, $\Delta\gamma$ $(= \dot{\gamma}\Delta t)$ is not marked as the the current or previous value because it is calculated for each increment separately and then used to update the state variables. Note that, plastic strain tensor $\boldsymbol{\varepsilon}^p$, accumulated plastic strain $\bar{\varepsilon}^p$ and the porosity f are the state (internal) variables of the constitutive model. Also, g_n functions are computed for the porosity value at the previous increment because the evolution of porosity is performed at the end of the subroutine in the current implementation.

Stress for the current increment can be obtained by combining Eqs. (2.11) and (2.15) as

$$\begin{aligned}\boldsymbol{\sigma}_{n+1} =& \kappa \left(tr(\boldsymbol{\varepsilon}_{n+1}) - tr(\boldsymbol{\varepsilon}^p_n) - \frac{1}{3}\frac{tr(\boldsymbol{\sigma}_{n+1})\Delta\gamma}{\bar{\sigma}_{n+1} g_{2,n}} \right) \mathbf{1} \\ &+ 2\mu \left(dev(\boldsymbol{\varepsilon}_{n+1}) - dev(\boldsymbol{\varepsilon}^p_n) - \Delta\gamma \frac{3}{2}\frac{dev(\boldsymbol{\sigma}_{n+1})}{\bar{\sigma}_{n+1} g_{1,n}} \right). \end{aligned} \tag{2.18}$$

Deviatoric and mean parts of the stress tensor should to be determined separately from Eq. (2.18) in order to be used in the yield potential. Mean part can be found by taking the trace of the equation,

$$tr(\boldsymbol{\sigma}_{n+1}) = 3\kappa \left(tr(\boldsymbol{\varepsilon}_{n+1}) - tr(\boldsymbol{\varepsilon}^p_n) - \frac{1}{3}\frac{tr(\boldsymbol{\sigma}_{n+1})\Delta\gamma}{\bar{\sigma}_{n+1} g_{2,n}} \right). \tag{2.19}$$

Rearranging the terms yields the trace of the stress as

$$tr(\boldsymbol{\sigma}_{n+1}) = \frac{3\kappa \left(tr(\boldsymbol{\varepsilon}_{n+1}) - tr(\boldsymbol{\varepsilon}^p_n) \right)}{1 + \dfrac{\kappa\, \Delta\gamma}{\bar{\sigma}_{n+1}\, g_{2,n}}}. \tag{2.20}$$

The deviatoric part of the stress can be found similarly by taking the deviator of Eq. (2.18) which gives

$$dev(\boldsymbol{\sigma}_{n+1}) = 2\mu \left(dev(\boldsymbol{\varepsilon}_{n+1}) - dev(\boldsymbol{\varepsilon}^p_n) - \Delta\gamma \frac{3}{2}\frac{dev(\boldsymbol{\sigma}_{n+1})}{\bar{\sigma}_{n+1}\, g_{1,n}} \right). \tag{2.21}$$

Again, rearranging the terms yields deviatoric stress as

$$dev(\boldsymbol{\sigma}_{n+1}) = \frac{2\mu \left(dev(\boldsymbol{\varepsilon}_{n+1}) - dev(\boldsymbol{\varepsilon}^p_n) \right)}{1 + \dfrac{3\mu\Delta\gamma}{\bar{\sigma}_{n+1}\, g_{1,n}}}. \tag{2.22}$$

All the necessary derivations are completed for the stress update. The classical radial return algorithm is used for the numerical solution of constitutive equation. In the next section, the corresponding steps and derivations for the stress update are explained.

2.2.1 Radial return algorithm

Radial return or return mapping algorithms are among the most popular methods for the calculation of constitutive equations. The algorithm includes elastic predictor (trial) and plastic corrector steps. In the prediction step, the idea is to guess a stress state assuming the incremental strain is totally elastic for the current step. Then,

the trial stress is checked using the yield surface defined by the yield potential. The surface is the elastic limit for the model; thus, stress at the end of the calculation has to be inside or on the yield surface. If the trial stress is inside the surface, then the prediction is correct, and the stress is equal to the trial stress. Suppose the trial stress surpasses the yield surface. In that case, the current increment is a plastic one. Stress for the current increment has to be corrected considering the evolution of the yield surface based on the strain hardening and other constitutive variables. Correction usually requires an iterative solution due to the nonlinearity of the yield potential. This step brings the trial stress back to the yield surface, which is the radial return part of the algorithm.

For the current porous plasticity model, necessary steps are explained starting from the prediction step. Elastic predictor stress can be written by taking $\Delta\gamma = 0$,

$$\boldsymbol{\sigma}_{n+1}^{trial} = \kappa(tr(\boldsymbol{\varepsilon}_{n+1}) - tr(\boldsymbol{\varepsilon}_n^p))\mathbf{1} + 2\mu(dev(\boldsymbol{\varepsilon}_{n+1}) - dev(\boldsymbol{\varepsilon}_n^p)) \tag{2.23}$$

which means purely elastic behavior is assumed for the current deformation increment. Using the trial stress, trial yield function can be written as

$$\phi_{n+1}^{trial} = \sqrt{\frac{3}{2}\frac{dev(\boldsymbol{\sigma}_{n+1}^{trial}) : dev(\boldsymbol{\sigma}_{n+1}^{trial})}{g_{1,n}(f_n)} + \frac{1}{9}\frac{(tr(\boldsymbol{\sigma}_{n+1}^{trial}))^2}{g_{2,n}(f_n)}} - \sigma_{y,n}. \tag{2.24}$$

The state of the material is determined by checking whether the yield function is bigger or smaller than 0. If $\phi_{n+1}^{trial} \leqslant 0$ then the material behaves elastically and $\Delta\gamma = 0$. If $\phi_{n+1}^{trial} > 0$, step is then called plastic step, and plastic multiplier, $\Delta\gamma$, needs to be computed so that $\phi_{n+1} = 0$ which indicates that stress state is returned back to the yield surface. Note that, porosity functions $g_{1,n}$, $g_{2,n}$ and σ_y are calculated using the state variables (f_n and $\boldsymbol{\varepsilon}_n^p$) at the previous increment; thus, they are not marked as trial values.

It is important to note that, due to the coaxiality of the trial deviatoric stress, $dev(\boldsymbol{\sigma}_{n+1}^{trial})$, and the final deviatoric stress, $dev(\boldsymbol{\sigma}_{n+1})$, the deviatoric part of the flow direction is known from the elastic prediction stress, as

$$dev(\boldsymbol{n}_{n+1}) = dev(\boldsymbol{n}_{n+1}^{trial}) \tag{2.25}$$

where $\boldsymbol{n} = \partial\phi/\partial\boldsymbol{\sigma}$. The sufficient condition for coaxiality is

$$dev(\boldsymbol{\sigma}_{n+1}) : dev(\boldsymbol{\sigma}_{n+1}^{trial}) = dev(\boldsymbol{\sigma}_{n+1}^{trial}) : dev(\boldsymbol{\sigma}_{n+1}). \tag{2.26}$$

This condition can be satisfied by using the Eqs. (2.22) and (2.23) as

$$\begin{aligned}&\left(\frac{2\mu\,(dev(\boldsymbol{\varepsilon}_{n+1})-dev(\boldsymbol{\varepsilon}^p_n))}{1+\frac{3\mu\Delta\gamma}{\bar{\sigma}_{n+1}\,g_{1,n}}}\right):(2\mu(dev(\boldsymbol{\varepsilon}_{n+1})-dev(\boldsymbol{\varepsilon}^p_n)))=\\&(2\mu(dev(\boldsymbol{\varepsilon}_{n+1})-dev(\boldsymbol{\varepsilon}^p_n))):\left(\frac{2\mu\,(dev(\boldsymbol{\varepsilon}_{n+1})-dev(\boldsymbol{\varepsilon}^p_n))}{1+\frac{3\mu\Delta\gamma}{\bar{\sigma}_{n+1}\,g_{1,n}}}\right).\end{aligned}\tag{2.27}$$

Then coaxiality can be shown as

$$\begin{aligned}&\left(\frac{4\mu}{1+\frac{3\mu\Delta\gamma}{\bar{\sigma}_{n+1}\,g_{1,n}}}\right)(dev(\boldsymbol{\varepsilon}_{n+1}):dev(\boldsymbol{\varepsilon}_{n+1})-dev(\boldsymbol{\varepsilon}^p_n):dev(\boldsymbol{\varepsilon}_{n+1})\\&-dev(\boldsymbol{\varepsilon}_{n+1}):dev(\boldsymbol{\varepsilon}^p_n)+dev(\boldsymbol{\varepsilon}^p_n):dev(\boldsymbol{\varepsilon}^p_n))=\\&\left(\frac{4\mu}{1+\frac{3\mu\Delta\gamma}{\bar{\sigma}_{n+1}\,g_{1,n}}}\right)(dev(\boldsymbol{\varepsilon}_{n+1}):dev(\boldsymbol{\varepsilon}_{n+1})-dev(\boldsymbol{\varepsilon}^p_n):dev(\boldsymbol{\varepsilon}_{n+1})\\&-dev(\boldsymbol{\varepsilon}_{n+1}):dev(\boldsymbol{\varepsilon}^p_n)+dev(\boldsymbol{\varepsilon}^p_n):dev(\boldsymbol{\varepsilon}^p_n)).\end{aligned}\tag{2.28}$$

In addition, for the current implementation, hydrostatic part of the flow direction is assumed to be known from the trial stress as well (i.e. $tr(\boldsymbol{n}_{n+1})=tr(\boldsymbol{n}^{trial}_{n+1})$).

In the algorithm, if the step is found to be elastic ($\phi^{trial}_{n+1}\leq 0$ and $\Delta\gamma=0$) then state variables do not change and stress is equal to the trial stress as follows:

$$\begin{aligned}\boldsymbol{\varepsilon}^p_{n+1}&=\boldsymbol{\varepsilon}^p_n,\\\bar{\varepsilon}^p_{n+1}&=\bar{\varepsilon}^p_n,\\f_{n+1}&=f_n,\\\boldsymbol{\sigma}_{n+1}&=\boldsymbol{\sigma}^{trial}_{n+1}.\end{aligned}\tag{2.29}$$

Otherwise, the trial stress is beyond the yield surface ($\phi^{trial}_{n+1}>0$) and the plastic correction step has to be performed. This requires the calculation of incremental flow multiplier, $\Delta\gamma$. Since the yield function is nonlinear, the Newton-Raphson method is used for the computation in the subroutine. The derivative $\partial\phi_{n+1}/\partial\Delta\gamma$ is required for the iterative solution. In order to find the derivative, yield function in the current step is written in an open form using Eqs. (2.1) (2.20) (2.22),

$$\phi_{n+1}=\sqrt{\frac{3}{2}\frac{dev(\boldsymbol{\sigma}^{trial}_{n+1}):dev(\boldsymbol{\sigma}^{trial}_{n+1})}{g_{1,n}\left(1+\dfrac{3\mu\,\Delta\gamma}{\bar{\sigma}_{n+1}\,g_{1,n}}\right)^2}+\frac{1}{9}\frac{(tr(\boldsymbol{\sigma}^{trial}_{n+1}))^2}{g_{2,n}\left(1+\dfrac{\kappa\,\Delta\gamma}{\bar{\sigma}_{n+1}\,g_{2,n}}\right)^2}}-\sigma_{y,n+1}.\tag{2.30}$$

The terms in the denominator are identified as

$$G = 1 + \frac{3\mu\,\Delta\gamma}{\sigma_{y,n+1}\,g_{1,n}},\quad H = 1 + \frac{\kappa\,\Delta\gamma}{\sigma_{y,n+1}\,g_{2,n}} \tag{2.31}$$

for simplicity of the derivation and also $\bar{\sigma} = \sigma_y$ because $\phi = \bar{\sigma} - \sigma_y = 0$ in a plastic increment. Therefore, algorithmic yield function can be written as

$$\phi_{n+1} = \sqrt{\frac{3}{2}\frac{dev(\boldsymbol{\sigma}^{trial}_{n+1}) : dev(\boldsymbol{\sigma}^{trial}_{n+1})}{g_{1,n}G^2} + \frac{1}{9}\frac{(tr(\boldsymbol{\sigma}^{trial}_{n+1}))^2}{g_{2,n}H^2}} - \sigma_{y,n+1}. \tag{2.32}$$

Then, the derivative, $\partial\phi_{n+1}/\partial\Delta\gamma$, can be found as follows:

$$\begin{aligned}\frac{\partial\phi_{n+1}}{\partial\Delta\gamma} =& \frac{-1}{\bar{\sigma}}\left[\frac{9\mu}{2}\frac{\boldsymbol{\sigma}'^{,trial}_{n+1} : \boldsymbol{\sigma}'^{,trial}_{n+1}}{\sigma^2_{y,n+1}\,g^2_{1,n}\,G^3}\left(\sigma_{y,n+1} - \frac{\partial\sigma_{y,n+1}}{\partial\Delta\gamma}\Delta\gamma\right)\right.\\ &\left. + \frac{\kappa}{9}\frac{(tr(\boldsymbol{\sigma}^{trial}_{n+1}))^2}{\sigma^2_{y,n+1}\,g^2_{2,n}\,H^3}\left(\sigma_{y,n+1} - \frac{\partial\sigma_{y,n+1}}{\partial\Delta\gamma}\Delta\gamma\right)\right] - \frac{\partial\sigma_{y,n+1}}{\partial\Delta\gamma}\end{aligned} \tag{2.33}$$

where

$$\sigma_{y,n+1} = \left(1 + \frac{E\bar{\varepsilon}^p_{n+1}}{\sigma_0}\right)^n,\quad \frac{\partial\sigma_y}{\partial\Delta\gamma} = nE\left(1 + \frac{E\bar{\varepsilon}^p_{n+1}}{\sigma_0}\right)^{n-1} \tag{2.34}$$

for the exponential hardening relation used in the numerical examples in the current work and superscript n is the hardening exponent.

Algorithm 1: Newton-Raphson Algorithm for the calculation of $\Delta\gamma$

```
Initilize Δγ = 0
while Residual < Tolerance do
    Update ε̄^p_{n+1} (Eq. 2.16)
    Calculate σ_{y,n+1} and ∂σ_{y,n+1}/∂Δγ (Eq. 2.34)
    Find the residual from Res = |φ_{n+1}| (Eq. 2.32)
    Calculate ∂φ_{n+1}/∂Δγ (Eq. 2.33)
    Update Δγ ← (Δγ − Res/(∂φ_{n+1}/∂Δγ))
end
```

Algorithm initiates with $\Delta\gamma = 0$, computes the variables in Eqs. (2.33)-(2.34) and updates $\Delta\gamma$ as shown in the Algorithm 1. Iterations continue until $|\phi_{n+1}| < Tolerance$ from Eq. (2.32). Tolerance value used in the calculations is 10^{-12}. After the iterations are complete, $\Delta\gamma$ is found, and state variables can be updated with the following

relations.

$$\begin{aligned} \boldsymbol{\varepsilon}^p_{n+1} &= \boldsymbol{\varepsilon}^p_n + \Delta\gamma \boldsymbol{n}_{n+1}, \\ \bar{\varepsilon}^p_{n+1} &= \bar{\varepsilon}^p_n + \Delta\gamma, \\ f_{n+1} &= \frac{f_n + \Delta\gamma \; tr(\boldsymbol{n}_{n+1})}{1 + \Delta\gamma \; tr(\boldsymbol{n}_{n+1})} \end{aligned} \tag{2.35}$$

where the plastic flow direction is

$$\boldsymbol{n}_{n+1} = \left(\frac{3}{2} \frac{dev(\boldsymbol{\sigma}^{trial}_{n+1})}{\bar{\sigma}^{trial}_{n+1} \, g_{1_n}} + \frac{1}{9} \frac{tr(\boldsymbol{\sigma}^{trial}_{n+1})}{\bar{\sigma}^{trial}_{n+1} \, g_{2_n}} \mathbf{1} \right). \tag{2.36}$$

Finally, stress tensor can be found from

$$\boldsymbol{\sigma}_{n+1} = \kappa \left(tr(\boldsymbol{\varepsilon}_{n+1}) - tr(\boldsymbol{\varepsilon}^p_{n+1}) \right) \mathbf{1} + 2\mu (dev(\boldsymbol{\varepsilon}_{n+1}) - dev(\boldsymbol{\varepsilon}^p_{n+1})). \tag{2.37}$$

Notice that the evolution of the porosity is not updated during the current increment which means that the yield surface in the current increment is found by using the porosity at the previous increment. Although the present implementation method is not the most rigorous method mathematically, using a sufficiently small step size solves this problem and yields a convergent solution for the numerical examples presented in the thesis.

Now, the update of the stress and the state variables are performed in the local material subroutine. However, the solution of nonlinear problems in mechanics with the finite element method requires an incremental-iterative solution scheme. The nonlinear problem is solved in small linear increments iteratively in the global finite element algorithm. Thus, the stiffness or the material tangent from the local model is necessary. Usually, the continuum or the consistent tangent modulus can be used as the material stiffness. The continuum modulus can be found directly by taking the derivative of the rate constitutive equations while the consistent tangent is found from the differentiation of algorithmic constitutive equations. For the current model, the consistent tangent modulus is used but differentiation is performed numerically as explained in the following section due to the complicated formulation.

2.2.2 Calculation of the numerical tangent modulus

Using a consistent tangent modulus provides an optimal convergence rate for the global finite element solver based on the Newton's method (see [75]). It is computed

here numerically using the perturbation technique due to its complicated derivation in the current model. With this method, 6 additional stress calculations have to be made. Thus, it is computationally more costly but brings simplification to the implementation of the model. Consistent tangent modulus, which is a 4th order tensor, is normally calculated from

$$\mathbb{C}_{n+1} = \frac{\partial \boldsymbol{\sigma}_{n+1}}{\partial \boldsymbol{\varepsilon}_{n+1}}. \tag{2.38}$$

Instead of taking the derivative directly, it is approximated using

$$\mathbb{C}_{ij,\,n+1} \approx \frac{\Delta \boldsymbol{\sigma}_{i,\,n+1}}{\Delta \boldsymbol{\varepsilon}_{j,\,n+1}}, \tag{2.39}$$

in Voigt notation where Δ indicates the change between the values at the end of the increment ($\boldsymbol{\sigma}_{n+1}$, $\boldsymbol{\varepsilon}_{n+1}$) and at the perturbed state ($\boldsymbol{\sigma}^{per}_{n+1}$, $\boldsymbol{\varepsilon}^{per}_{n+1}$). In the subroutine, strains $\boldsymbol{\varepsilon}_{n+1}$ are perturbed with a very small value (10^{-10}), and stresses are recalculated at the perturbed state. Calculations are conducted following the same formulation and implementation explained previously; thus, no additional derivation is required to use the method. Then, the consistent tangent modulus can be found as

$$\mathbb{C}_{ij,\,n+1} = \frac{\boldsymbol{\sigma}^{per}_{i,\,n+1} - \boldsymbol{\sigma}_{i,\,n+1}}{\boldsymbol{\varepsilon}^{per}_{j,\,n+1} - \boldsymbol{\varepsilon}_{j,\,n+1}}. \tag{2.40}$$

It is essential to note here that perturbations have to be given in each strain component of $\boldsymbol{\varepsilon}_{n+1}$ separately because perturbing more than one component of strain would yield a stress state that includes the effect from both of the perturbed strains and calculation results in an incorrect tangent modulus. Therefore, for the 6 components of the modulus tensor in Voigt notation, only one perturbation state can be used, which implies that for a 6x6 modulus matrix, 6 additional perturbed stress states are required.

After presenting the implementation of the model as a material subroutine using the classical prediction-correction scheme with a numerical approximation of the consistent tangent modulus, the representative volume element (RVE) study under stress triaxiality is explained in the next chapter.

CHAPTER 3

RVE CALCULATIONS UNDER CONSTANT STRESS TRIAXIALITY

In this chapter, the modeling of the representative volume element (RVE) including a spherical void is discussed, and the application of constant triaxiality stress state is explained in detail. Finite element analyses of RVEs have been quite useful for the investigation of pore evolution in terms of both volume and shape of the voids as well as for addressing the stress carrying capacity of the ductile material. Here, the RVE is taken from a periodic array of cubic elements with spherical voids in the center, it is deformed under a constant triaxial stress state with proper boundary conditions. There are several different methods in the literature for porous RVE simulations under constant stress triaxiality. Some of the methods with 2D axisymmetric finite elements are discussed in [76] including the application of cyclic loads. In the current study, the method proposed in [77] is employed, which is a displacement controlled method performed on 3D models. The study in the thesis only covers the effect of stress triaxiality, T, on void evolution. However, the effect of Lode parameter can be studied in combination with T using the current methodology.

In Figure 3.1, voided RVE model is shown. Figure 3.1a demonstrates the unit cell with a spherical void in the center. By using the geometrical symmetry and boundary conditions, the one-eighth portion of the unit cell is modeled, as shown in Figures 3.1b and 3.1c. RVE model is meshed with 8 noded 3D hexahedral elements (C3D8) of ABAQUS. The number of elements for the model with an initial void volume fraction of $f_0 = 1\%$ is 4125, and for $f_0 = 0.1\%$ is 4831. The mesh density is increased at the near vicinity of the void with a node spacing of 0.01 and 0.02 mm at the edges of the void for $f_0 = 0.001$ and $f_0 = 0.01$, respectively, for an RVE with a 1 mm edge length. The initial edge length of the unit cell (see Figure 3.1a) is $2L_0$; hence, the

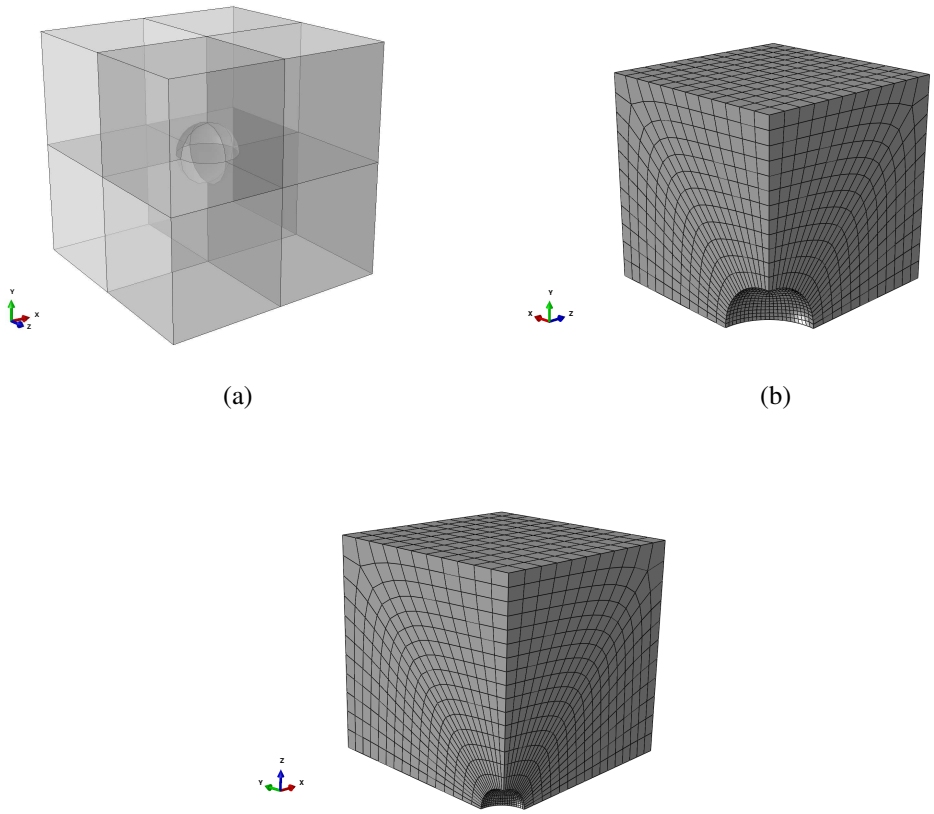

(a) (b)

(c)

Figure 3.1: (a) Complete RVE model for $f_0 = 0.01$ and finite element models of one-eighth of the RVE (b) $f_0 = 0.01$, (c) $f_0 = 0.001$.

edge length of the finite element models is L_0. The initial void volume fraction can be found by $f_0 = \pi r_0^3/(6L_0^3)$, where r_0 is the radius of the initial void. Moreover, the behavior of the matrix material is described by the classical von Mises plasticity theory with the material parameters presented in Table 4.1 and hardening relation in Eq. (4.1) in Chapter 4.

The stress state of the RVE can be characterized by stress triaxiality, T, and Lode parameter, L, defined as,

$$T = \frac{\Sigma_h}{\Sigma_{eq}}, \quad L = \frac{2\Sigma_{II} - \Sigma_I - \Sigma_{III}}{\Sigma_I - \Sigma_{III}} \tag{3.1}$$

where the hydrostatic and equivalent stresses are

$$\Sigma_h = \frac{\Sigma_{ii}}{3} = \frac{\Sigma_{11} + \Sigma_{22} + \Sigma_{33}}{3}, \tag{3.2}$$

$$\Sigma_{eq} = \frac{1}{\sqrt{2}}\sqrt{(\Sigma_{11}-\Sigma_{22})^2+(\Sigma_{11}-\Sigma_{33})^2+(\Sigma_{22}-\Sigma_{33})^2}. \tag{3.3}$$

Here Σ represents the so-called mesoscopic stress which describe the average stress response of the unit cell. Σ_I, Σ_{II}, Σ_{III} are the principal stresses defined as

$$\begin{aligned}
\Sigma_I &= \frac{\Sigma_{11}+\Sigma_{22}}{2} + \sqrt{\left(\frac{\Sigma_{11}-\Sigma_{22}}{2}\right)^2}, \\
\Sigma_{III} &= \frac{\Sigma_{11}+\Sigma_{22}}{2} - \sqrt{\left(\frac{\Sigma_{11}-\Sigma_{22}}{2}\right)^2}, \\
\Sigma_{II} &= \Sigma_{33}.
\end{aligned} \tag{3.4}$$

with $\Sigma_I \geq \Sigma_{II} \geq \Sigma_{III}$. Stress state can also be expressed in terms of non dimensional stress ratios as follows,

$$T = \frac{\sqrt{2}(1+\rho_{11}+\rho_{33})sign(\Sigma_{22})}{3\sqrt{(1-\rho_{11})^2+(1-\rho_{33})^2+(\rho_{33}-\rho_{11})^2}}, \tag{3.5}$$

$$L = -\frac{(1+\rho_{11}-2\rho_{33})sign(\Sigma_{22})}{\sqrt{(1-\rho_{11})^2}} \tag{3.6}$$

where stress ratios are $\rho_{11} = \Sigma_{11}/\Sigma_{22},\ \rho_{33} = \Sigma_{33}/\Sigma_{22}$. Since the applied mesoscopic stresses are only in the normal direction with respect to the unit cube surfaces for the current study, shear terms are zero and omitted in T and L expressions in Eqs. (3.3)-(3.6). Note that Lode parameter is taken as -1 for all RVE simulations in this study which implies $\rho_{11} = \rho_{33}$.

RVE is loaded utilizing three 1D axial elements (CONN3D2) of ABAQUS. These elements act as linear springs and they are inserted between the dummy nodes $M_1 - N_1$, $M_1 - N_2$ and $M_1 - N_3$ as shown in the Figure 3.2. Dummy nodes are used to control forces in the springs utilizing a multi-point constraint user subroutine (MPC subroutine of Abaqus [74]). Nodes are created outside of the RVE, ensuring that the spring elements are parallel with the coordinate axes, and they are not a part of the finite element mesh. Forces in the springs are transferred to the cell surfaces with a displacement coupling between surface nodes and node M_1. This constraint is enforced with the "equation constraint" of ABAQUS. Node sets are created from the nodes at the outer surfaces which are named as x_{surf}, y_{surf} and z_{surf} (see Figure 3.3). Displacements of these nodes are coupled to the corresponding displacements

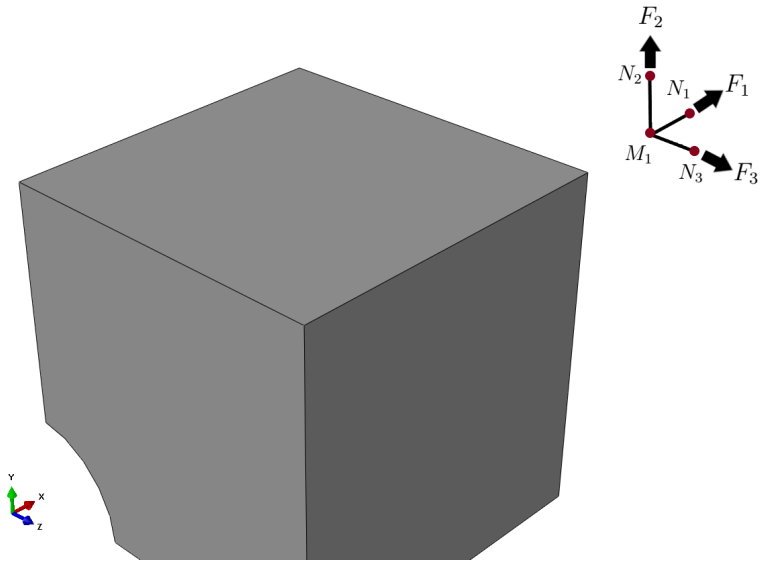

Figure 3.2: Positions of the dummy nodes and corresponding spring forces.

of node M_1 as

$$u^1_{M_1} = u^1_{x_{surf}}, \quad u^2_{M_1} = u^2_{y_{surf}}, \quad u^3_{M_1} = u^3_{z_{surf}}. \tag{3.7}$$

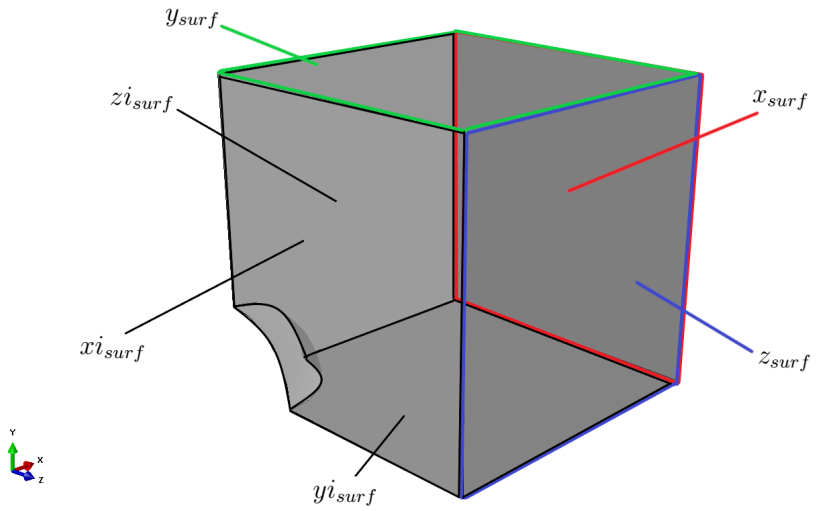

Figure 3.3: Surfaces used for boundary conditions.

With the displacement coupling, the outer surfaces stay straight and aligned with the coordinate axes during the deformation. For the inner boundaries of the cell near the void (xi_{surf}, yi_{surf}, zi_{surf}, see Figure 3.3), symmetry boundary conditions are

applied, as

$$u^1_{xi_{surf}} = 0, \;\; u^2_{yi_{surf}} = 0, \;\; u^3_{zi_{surf}} = 0, \tag{3.8}$$

where the superscripts 1, 2 and 3 corresponds to the x, y and z directions, respectively.

The mesoscopic stresses acting on the RVE can be represented using the spring forces as

$$\Sigma_{11} = \frac{F_1}{A_1}, \; \Sigma_{22} = \frac{F_2}{A_2}, \; \Sigma_{33} = \frac{F_3}{A_3} \tag{3.9}$$

where A_1, A_2 and A_3 are the surface areas of x_{surf}, y_{surf} and z_{surf}, respectively. F_1, F_2 and F_3 are the forces created by the springs in the x, y and z directions. Forces and the areas are

$$\begin{aligned}
F_1 &= k(u^1_{N_1} - u^1_{M_1}), \; A_1 = (L_0 + u^2_{M_1})(L_0 + u^3_{M_1}), \\
F_2 &= k(u^2_{N_2} - u^2_{M_1}), \; A_2 = (L_0 + u^1_{M_1})(L_0 + u^3_{M_1}), \\
F_3 &= k(u^3_{N_3} - u^3_{M_1}), \; A_3 = (L_0 + u^1_{M_1})(L_0 + u^2_{M_1}),
\end{aligned} \tag{3.10}$$

where k is the spring constant (i.e. elastic modulus of the axial element). Constant stress ratios can be written using the Eqs. (3.9) and (3.10), as

$$\begin{aligned}
\rho_{11} &= \frac{\Sigma_{11}}{\Sigma_{22}} = \frac{F_1}{A_1}\frac{A_2}{F_2} = \frac{A_2(u^1_{N_1} - u^1_{M_1})}{A_1(u^2_{N_2} - u^2_{M_1})}, \\
\rho_{33} &= \frac{\Sigma_{33}}{\Sigma_{22}} = \frac{F_3}{A_3}\frac{A_2}{F_2} = \frac{A_2(u^3_{N_3} - u^3_{M_1})}{A_3(u^2_{N_2} - u^2_{M_1})}
\end{aligned} \tag{3.11}$$

Note that spring constant k is not in the equation; however, it affects the convergence rate of the solution. k is taken as $E/10$, as suggested by Tekoğlu [77], where E is the elastic modulus of the matrix material. Finally, the multi-point constraint equations are

$$\begin{aligned}
\rho_{11}(u^2_{N_2} - u^2_{M_1}) - \frac{L_0 + u^1_{M_1}}{L_0 + u^2_{M_1}}(u^1_{N_1} - u^1_{M_1}) = 0, \\
\rho_{33}(u^2_{N_2} - u^2_{M_1}) - \frac{L_0 + u^3_{M_1}}{L_0 + u^2_{M_1}}(u^3_{N_3} - u^3_{M_1}) = 0
\end{aligned} \tag{3.12}$$

from Eqs. (3.11) and (3.10). The two equations given in (3.12) are needed to be satisfied with the Abaqus MPC subroutine. There are 5 unknowns $u^1_{M_1}$, $u^2_{M_1}$, $u^3_{M_1}$, $u^1_{N_1}$ and $u^3_{N_3}$ in Eq. (3.12) and $u^2_{N_2}$ is the prescribed displacement value. Notice that only 3 nodes and 4 displacement values are required to solve each equation (M_1, N_1 and

N_2 for the first equation, M_1, N_3 and N_2 for the second equation). For the present application, N_2 & M_1 are the independent nodes and N_1 & N_3 are the dependent nodes because their displacement values are calculated and enforced in the MPC subroutine. The current method is a displacement controlled approach that uses spring elements and multi point constraints. Alternatively, the Riks method, with traction boundary conditions, can also be employed to apply constant stress triaxiality on an RVE model (see e.g. [78, 79]).

Results from the RVE analysis are obtained by volume averaging stress components at each integration point in the finite element model by using the relation between the mesoscopic stress, Σ_{ij}, and the microscopic local stress, σ_{ij}, as

$$\Sigma_{ij} = \frac{1}{V} \int_V \sigma_{ij} dV \tag{3.13}$$

where V is the volume of the RVE. Therefore, for a finite element model, mesoscopic stress can be found by volume averaging the local stress components in the RVE, as

$$\Sigma_{ij} = \sum_{e=1}^{N} \left(\sum_{q=1}^{p} \sigma_{ij}^{q,e} v^{q,e} \right) / V \tag{3.14}$$

where σ_{ij} is the local stress, N is the total number of elements, p is the number of integration points in an element (8 for an C3D8 element) and v is the local volume at an integration point. The total RVE volume, V, can be computed by summation of local v values. The mesoscopic strains can be found by

$$E_{11} = ln\left(\frac{l_1}{L}\right),\ E_{22} = ln\left(\frac{l_2}{L}\right),\ E_{33} = ln\left(\frac{l_3}{L}\right) \tag{3.15}$$

where l and L are the final and initial edge lengths of the RVE model, respectively. Averaging is done through a Python script written based on the script given in [80]. Porosity value is obtained from the same script using the following equation:

$$f = (L_0 + u^1_{M_1})(L_0 + u^2_{M_1})(L_0 + u^3_{M_1}) - V. \tag{3.16}$$

Parameter sets for the RVE study are listed below.

- $f_0 = 0.01,\ 0.001$: typical initial porosity levels for metal alloys.
- $T = 0.35,\ 0.66,\ 0.75,\ 1,\ 2,\ 3$: stress triaxiality range covers most of the stress states that ductile metals encounter during deformation.

- $n = 0.1,\ 0.2$: two different hardening exponents are tested to address the performance of the porous plasticity model under different hardening conditions.

Simulations are performed with Abaqus/Standard implicit finite element solver with constants step size, $\Delta t = 0.001$, and total time, $t_{total} = 1$.

In the next chapter, numerical results of the RVE analysis and the porous plasticity model are presented. An extension of the current model is proposed based on the RVE results and comparisons are made with the extended model and the well-known GTN model. In addition, the performance of the extended model is addressed through uniaxial tension simulations of blunt notched and smooth specimens.

CHAPTER 4

RESULTS AND DISCUSSION

In this chapter, the numerical analysis conducted on the presented RVEs are addressed together with the results from the presented porous plasticity and the GTN models. An extension of the current model is proposed for capturing better fit with the RVE calculations. Moreover, further simulations are done on blunt notched and smooth specimens using the porous plasticity, GTN and uncoupled Johnson-Cook models for capturing ductile failure. The fracture locus employed in the Johson-Cook model is obtained from the RVE analysis. The fracture strain values are taken at the onset of void coalescence in the RVE results, and the variables in the Johnson-Cook model are obtained through curve fitting. Note that the model implemented in the thesis is referred to as the porous plasticity model or the porous model in this chapter.

4.1 Material parameters

In all finite element calculations, the following exponential relation is employed to describe the isotropic hardening behavior of the material in both the porous plasticity model and the matrix material of the RVE.

$$\frac{\sigma_y}{\sigma_0} = \left(1 + \frac{E\bar{\varepsilon}^p}{\sigma_0}\right)^n \tag{4.1}$$

where σ_0 is the initial yield stress, n is the hardening exponent, $\bar{\varepsilon}^p$ is accumulated plastic strain ($\bar{\varepsilon}^p = \int_0^t ||\dot{\boldsymbol{\varepsilon}}^p(\tau)||d\tau$) which is one of the state variables of the constitutive model and E is Young's modulus. Material parameters are presented in Table 4.1. Two different hardening exponents ($n = 0.1,\ 0.2$) are used to investigate the performance of the model at different hardening conditions. Also, the material is linear elastic up to the initial yield stress, σ_0.

Table 4.1: Material parameters

E/σ_0	n	E	ν
300	0.1, 0.2	70000 [MPa]	0.3

The conversion from the Young's modulus, E, and Poisson's ratio, ν, to the bulk modulus, κ, and shear modulus, μ, which are used in the porous plasticity model, can be done using the following relations

$$\kappa = \frac{E}{3(1-2\nu)}, \quad \mu = \frac{E}{2(1+\nu)}. \tag{4.2}$$

Note that in the RVE analysis the classical J2 plasticity model with the isotropic hardening relation in 4.1 is employed. From this study both the evolution of pore volume fraction and the mesoscopic response of the material are obtained. Then, the analysis of the porous plasticity and the GTN models are conducted under the same conditions.

4.2 Single element response of the porous plasticity model

The porous plasticity model and the numerical implementation are tested and compared with the built-in J2 plasticity model of Abaqus. A single 3D finite element (C3D8) is considered under uniaxial tension/compression and pure shear conditions, as illustrated in Figure 4.1. Model is a unit cube with $1 \times 1 \times 1$ mm dimensions. Uniaxial loading is tested with both displacement and traction boundary conditions. For the hardening exponent, $n = 0.1$ is used. Hardening is provided to Abaqus in a user hardening subroutine (UHARD). Calculations are done with a constant step size of 0.001 using the standard implicit solver. Moreover, calculation times are also compared between the present implementation and the plasticity model of Abaqus.

Left, back and bottom faces of the element are fixed in their respective normal directions as shown in Figure 4.1, and displacement/traction is applied to the right face with the normal x to simulate a uniaxial deformation behavior. For the displacement boundary condition, 0.4, -0.2 and 0.1 mm are used as displacement values in the

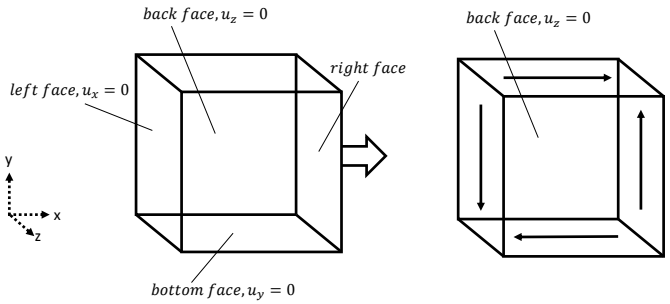

Figure 4.1: Single element under uniaxial (left) and pure shear (right) loads.

x-direction, which applies an arbitrary tension-compression to the element. The traction boundary condition is handled similarly. The applied tractions in the x-direction are 300, -350 and 400 MPa. Stress and strain data are extracted from the integration points. The results for the uniaxial test are shown in Figure 4.2. In Figures 4.2a and 4.2b, the stress versus strain responses obtained from displacement and traction boundary conditions are shown, respectively. It can be seen that the UMAT implementation of the model yields exactly the same results as the built-in plasticity model of Abaqus at 0 initial porosity. Results for $f_0 = 0.05$ is also plotted to show the effect of having a high porosity value. The yield stress decreases, and the model generally shows a similar trend but at a damaged state. Note that the evolution of the porosity is very small and can be neglected in uniaxial loading conditions; thus, the porosity induced damage only comes from the initial porosity. Under the traction boundary condition, the present implementation at $f_0 = 0$ again yields the same result. $f_0 = 0.05$ is not included for the traction boundary condition results because, at a damaged state, the material cannot carry the same load as in undamaged conditions, and convergence cannot be achieved.

Pure shear is applied to the element through prescribed displacement boundary conditions. Each face of the element is displaced 0.2 mm in the directions, as shown in Figure 4.1 while the back face with the normal z is fixed in the z-direction. Resultant shear stress-strain response is shown in Figure 4.3. It can be concluded that the porous plasticity model can predict the same results as the built-in Abaqus plasticity model at $f_0 = 0$. Furthermore, the decrease in the yield stress and overall shear stress capacity of the element is reduced at $f_0 = 0.05$. Under the effect of pure shear, porosity does not change for the current model.

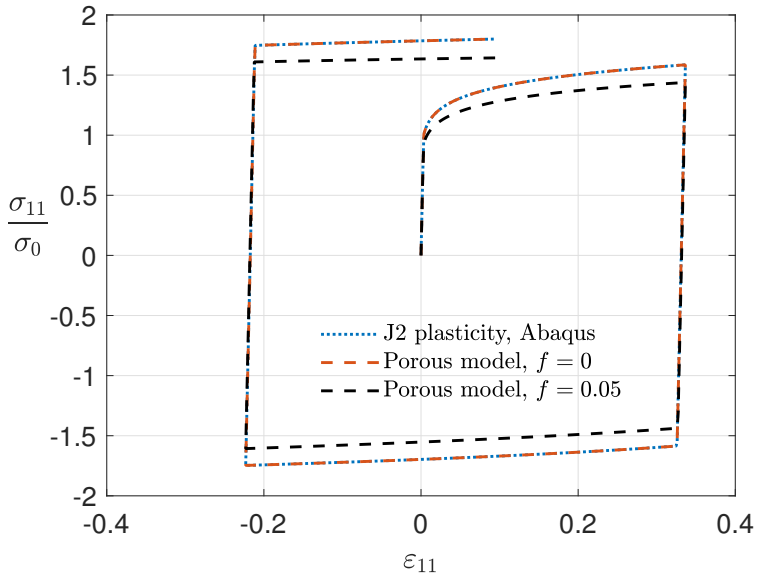

(a) Displacement BC

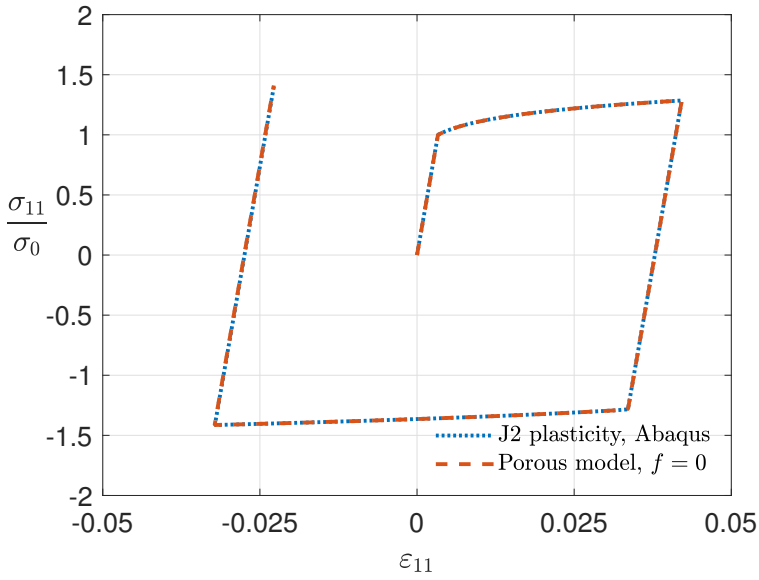

(b) Traction BC

Figure 4.2: Uniaxial stress-strain relation of the porous plasticity model and Abaqus J2 plasticity model. (a) Under prescribed displacement, (b) under prescribed surface traction

The current implementation of the porous plasticity model at $f_0 = 0$ and the built-in J2 plasticity model of Abaqus are compared in terms of total CPU times in Table 4.2. Although at zero porosity, both models solve the exact same constitutive equa-

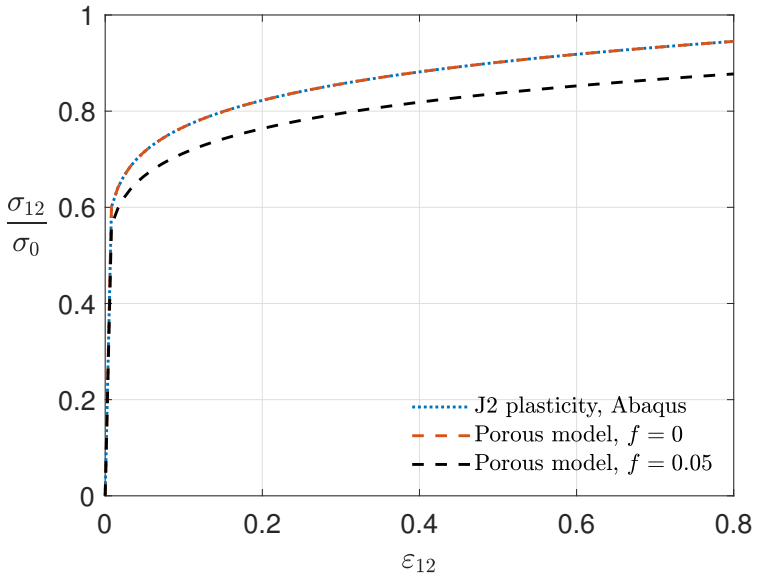

Figure 4.3: Stress-strain relation of the porous plasticity model and Abaqus J2 plasticity model under pure shear.

tions, present implementation consistently takes a longer time to solve compared to the Abaqus constitutive model. The main reason behind this difference is that the porous implementation calculates the tangent modulus numerically in the subroutine by making 6 additional stress calculations, while for the classical implementation of the J2 plasticity, the tangent modulus can be found in an open form.

Table 4.2: Simulation times of the porous plasticity model and the Abaqus J2 plasticity model.

CPU times (sec)	Uniaxial (disp)	Uniaxial (trac)	Pure shear
Porous model	19.5	21.5	7.1
Abaqus J2 model	16.5	19.0	6.5

Additional finite element calculations are performed with finite rotations without applying any strain to the element in order to ensure that the model does not yield any stress for rotation only. Moreover, the same uniaxial tension and pure shear loads are applied in different directions, and the stress-strain responses are found to be identical to the ones presented previously. The results indicate that the present implementation of the porous plasticity model works as intended, and the numerical calculation of the

tangent modulus is done correctly. After validating the implementation and UMAT subroutine, the RVE analysis results are presented in the following section.

4.3 Results from the RVE analysis

Firstly, the RVE calculation methodology is validated through error calculations performed using the prescribed stress ratios, ρ_{11} & ρ_{33}, and the stress ratios obtained from the finite element calculations ρ_{11}^{FE} & ρ_{33}^{FE}. ρ_{11}^{FE} and ρ_{33}^{FE} corresponds to Σ_{11}/Σ_{22} and Σ_{33}/Σ_{22}, respectively. Figure 4.4 illustrates the variation of percent error with respect to equivalent strain for $f_0 = 0.01$, $n = 0.1$ and $L = -1$. The error is found to be less then 0.5×10^{-3} % for all equivalent strain values and the maximum error is obtained for $T = 3$.

Result from the finite element analysis of the RVE using hardening exponent $n = 0.1$ and Lode parameter $L = -1$ are plotted in Figures 4.5 and 4.6 at two different initial porosity levels. Figures 4.5a and 4.6a show the equivalent stress-strain curves normalized with σ_0. The dominant effect of stress triaxiality on the ductility is evident for both $f_0 = 0.01$ and $f_0 = 0.001$. After a certain equivalent strain, the deformation mode changes and the radial growth of the RVE becomes negligible compared to the axial growth (i.e., $E_{11} = E_{33} = 0$ and $E_{22} \neq 0$). This point is also referred to as the onset of void coalescence, where internal necking starts in the ligaments that connect adjacent voids radially. The onset of uniaxial straining mode is marked by $\circ$ in the figures. Numerically, it is found when $\Delta E_{11}/\Delta E_{22}$ or $\Delta E_{33}/\Delta E_{22}$ is less than a tolerance value (=10^{-1}). After the uniaxial straining point, a sudden drop in the equivalent stress is observed. It can be seen that void coalescence starts at a relatively smaller equivalent strain for higher initial porosity.

Figures 4.5b and 4.6b illustrate the change in void volume fraction with equivalent strain. It is shown that below $T = 1$, void coalescence is not observed at $f = 0.001$; however, at $f = 0.01$, coalescence can occur even at $T = 0.75$ in the given equivalent strain range. The starting point of void coalescence is at an earlier equivalent strain value for $f_0 = 0.01$ compared to $f_0 = 0.001$, and also, the porosity value is significantly higher for all stress triaxiality values. Moreover, shift to void coalescence is

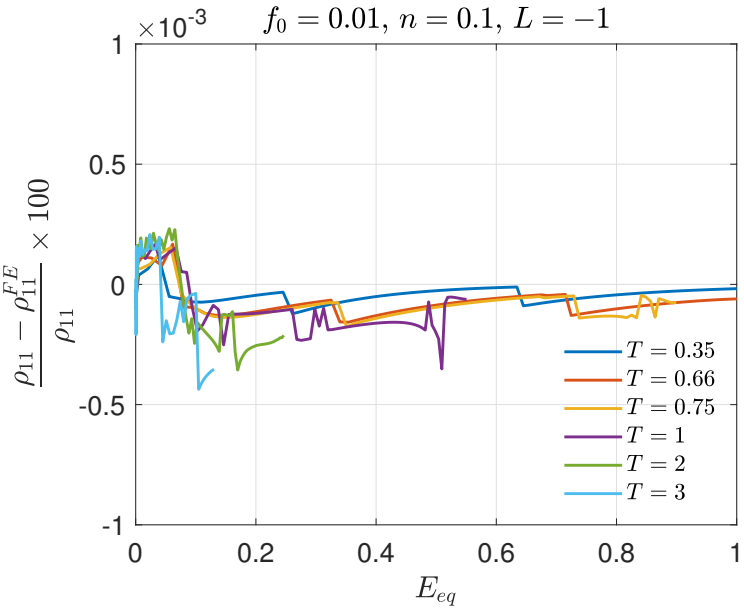

(a)

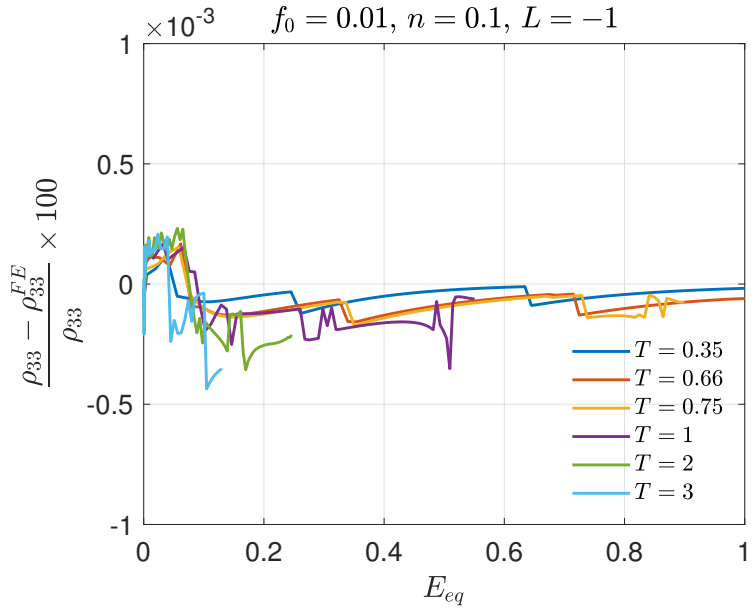

(b)

Figure 4.4: The percent error in stress ratios (a) ρ_{11} and (b) ρ_{33} vs equivalent strain for $f_0 = 0.01$, $n = 0.1$ and $L = -1$.

much sharper at $T = 0.75$ and $T = 1$ compared to $T = 2$ and $T = 3$. Note that, at a relatively small initial porosity, there is minimal void growth at triaxialities below 1, which also translates to almost no difference in ductility or stress carrying capacity (see Figure 4.6a). As the initial porosity increases, void growth became a prominent

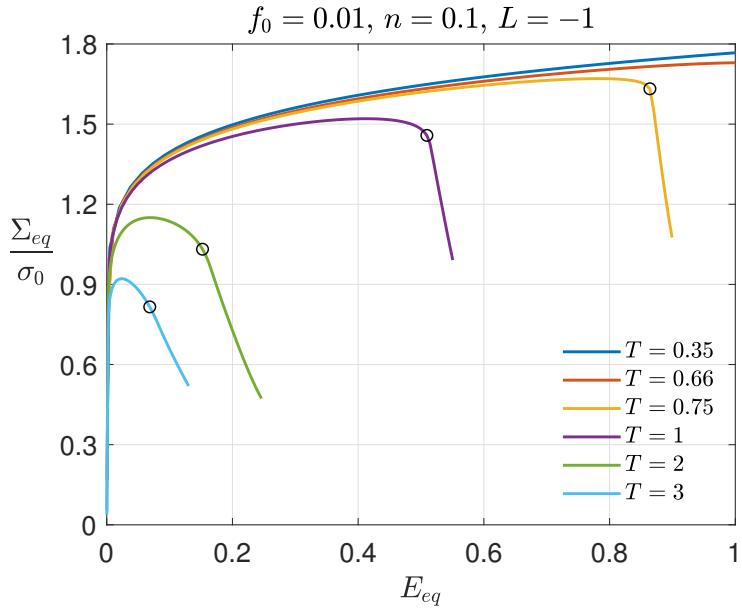

(a)

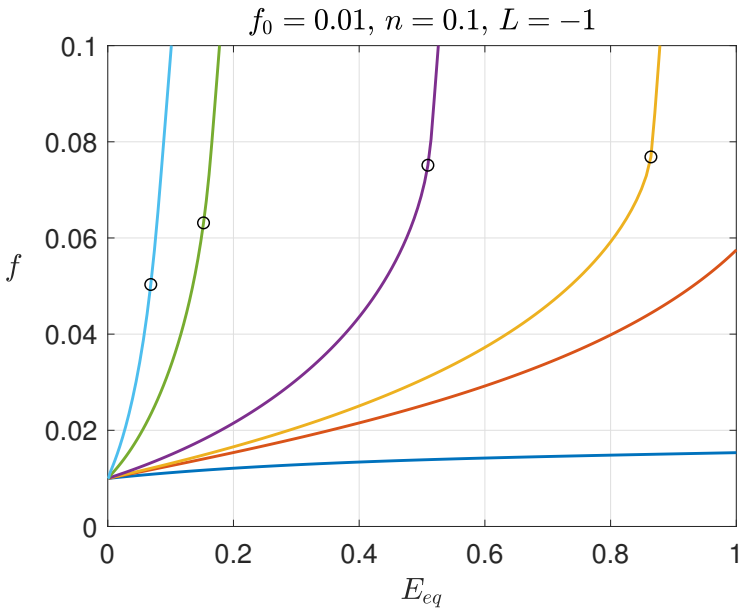

(b)

Figure 4.5: Results from the RVE simulations for $f_0 = 0.01$, $n = 0.1$ and $L = -1$. (a) Normalized equivalent stress strain relation, (b) void volume fraction, f, vs equivalent strain. The onset of uniaxial straining mode is marked by $\circ$.

event at low T values. Although increase of void volume fraction at $T = 0.66$ and below does not significantly affect equivalent stress, the importance of the growth would arise in a deformation process with evolving stress triaxiality.

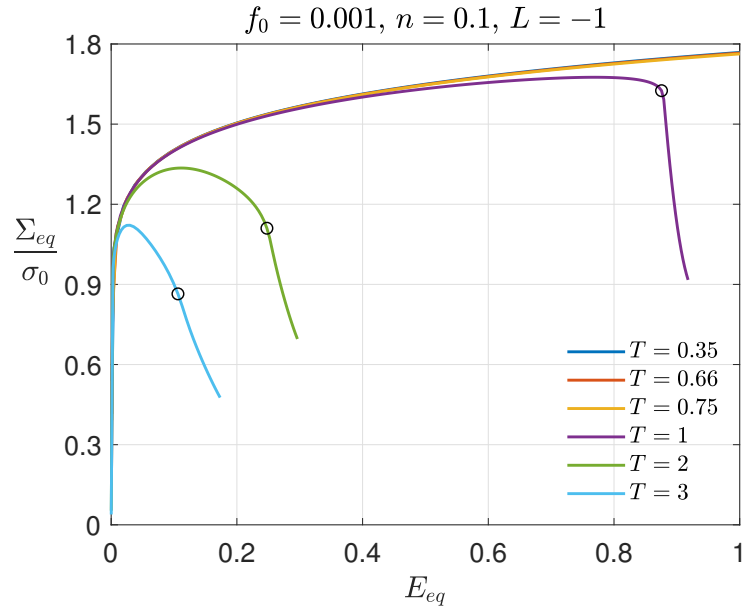

(a)

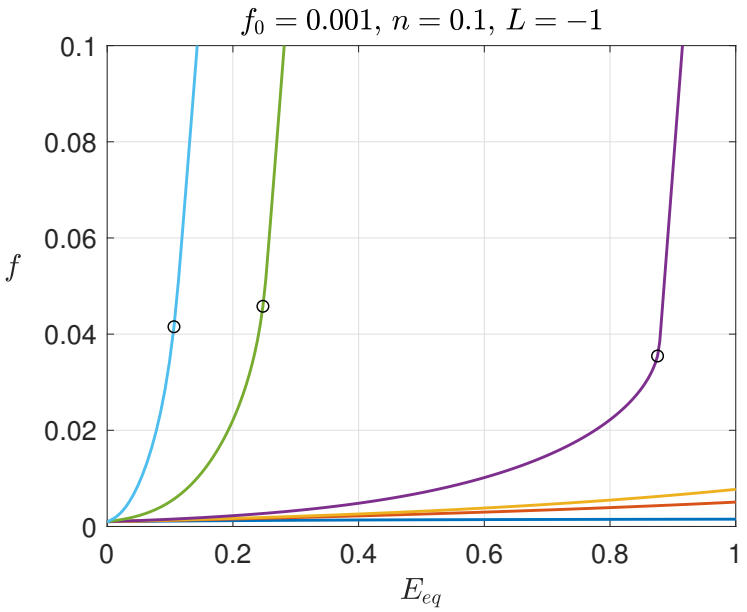

(b)

Figure 4.6: Results from the RVE simulations for $f_0 = 0.001$, $n = 0.1$ and $L = -1$. (a) Normalized equivalent stress strain relation, (b) void volume fraction, f, vs equivalent strain. The onset of uniaxial straining mode is marked by $\circ$.

The results for $n = 0.2$ are shown in Figures 4.7 and 4.8. Figures 4.7a and 4.8a demonstrate the equivalent stress-strain response and the porosity evolution is shown in Figures 4.7b and 4.8b. Similar conclusions can be made at this hardening exponent

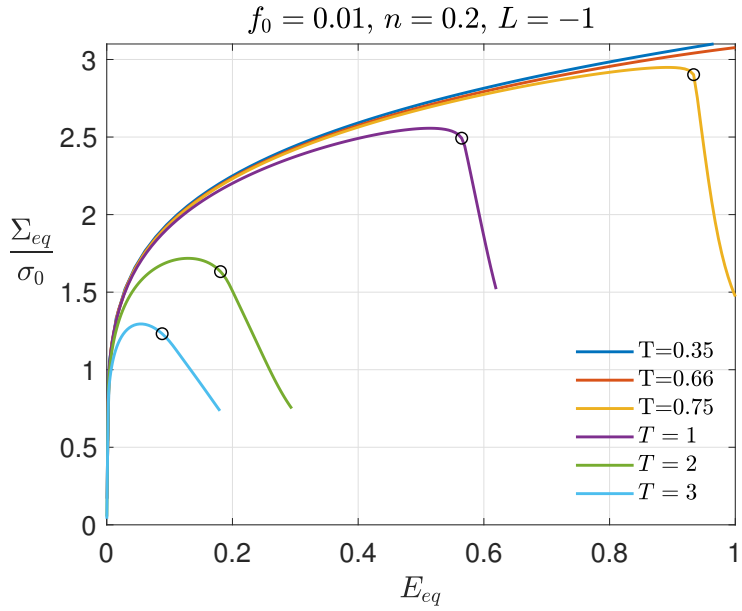

(a)

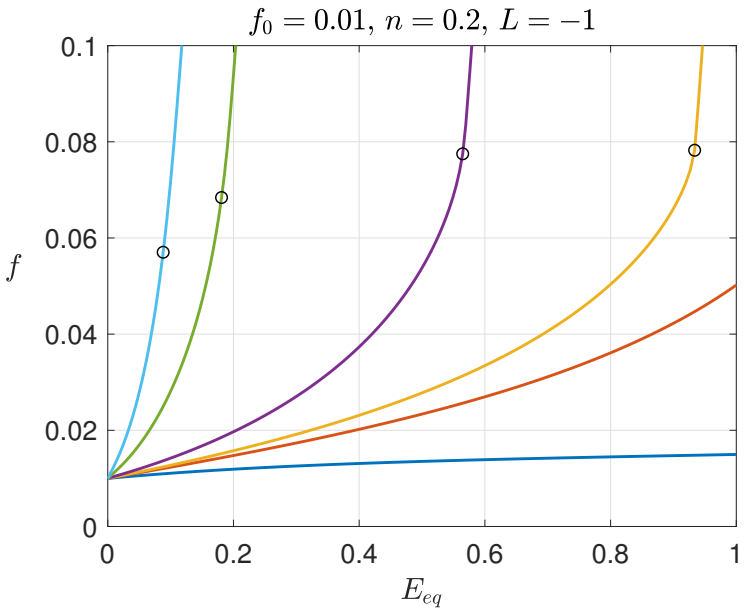

(b)

Figure 4.7: Results from the RVE simulations for $f_0 = 0.01$, $n = 0.2$ and $L = -1$. (a) Normalized equivalent stress strain relation, (b) void volume fraction, f, vs equivalent strain. The onset of uniaxial straining mode is marked by $\circ$.

compared to the $n = 0.1$. Additionally, as the hardening exponent is increased, void growth is slower and void coalescence starts at a higher equivalent strain value at the same initial porosity.

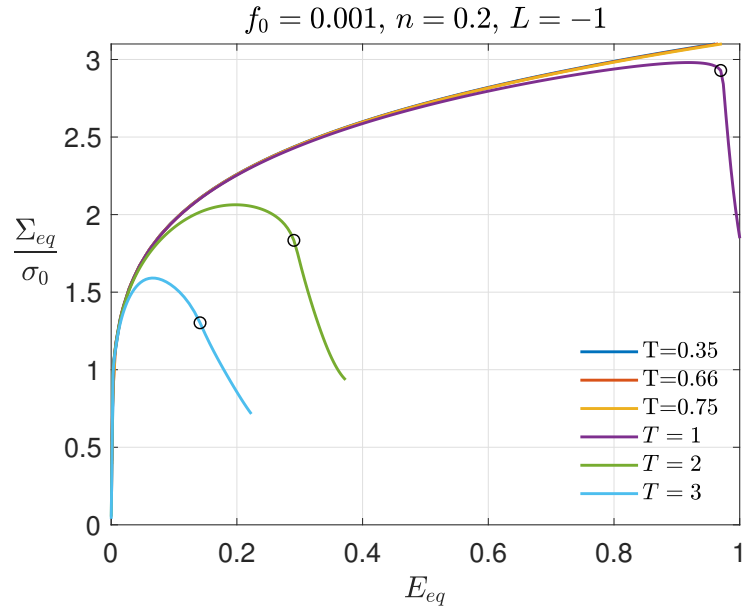

(a)

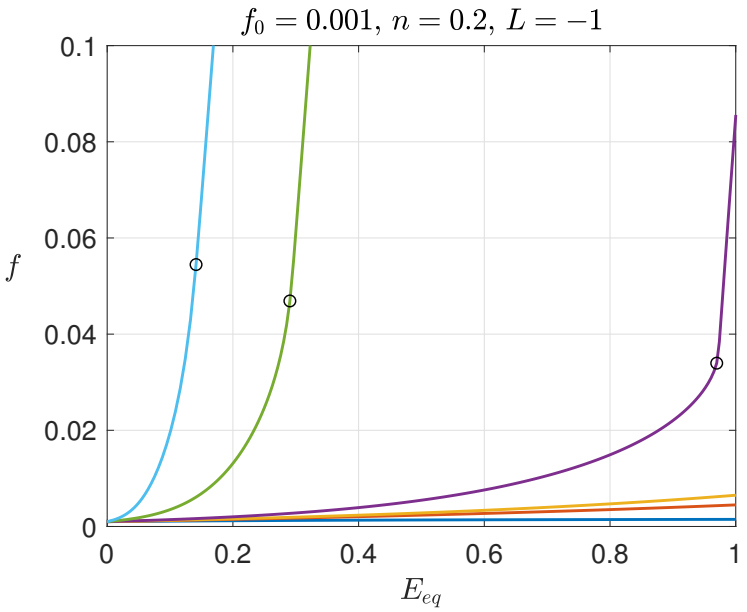

(b)

Figure 4.8: Results from the RVE simulations for $f_0 = 0.001$, $n = 0.2$ and $L = -1$. (a) Normalized equivalent stress strain relation, (b) void volume fraction, f, vs equivalent strain. The onset of uniaxial straining mode is marked by $\circ$.

The deformed shapes of the RVE's are shown in Figure 4.9 for $T = 0.35,\ 1,\ 3$. Figures are generated by mirroring the RVE, which is one-eighth of the complete voided unit cube. For $T = 1$ and 3, figures are taken at the point when the coalescence starts.

For $T = 0.35$, it is taken at an arbitrary point since there are small differences in plastic strain distribution throughout the deformation, and coalescence is not observed. In terms of shape change for $T = 0.35,\ 1$, it can be seen that void elongates in the vertical direction as the strain increases and takes a prolate shape, but for $T = 3$, void evolves into an oblate shape. Note that RVE's with voids under constant stress triaxiality has been studied thoroughly (see e.g. [38, 63, 77, 81]) and presented results are in well agreement with the literature.

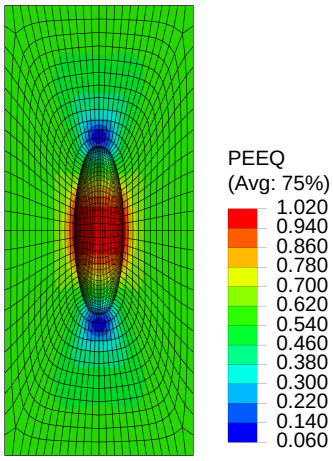

(a) $T = 0.35$

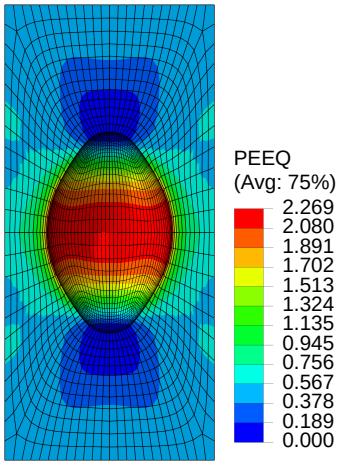

(b) $T = 1$

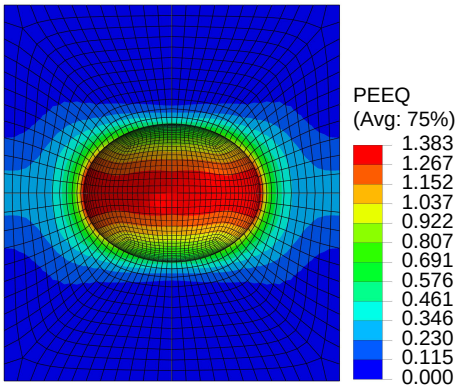

(c) $T = 3$

Figure 4.9: Equivalent plastic strain distribution and deformed shapes of the RVE's for $f_0 = 0.01$ at the onset of void coalescence for (b)(c) and at an arbitrary point for (a).

4.4 Comparison of the porous plasticity model and the RVE calculations

In this section, the results from the RVE calculations are compared with the ones from the current porous plasticity model. Results are obtained from a single 3D hexahedral element (C3D8) under constant stress triaxiality utilizing the same method as the RVE simulations. The voided model shown in the RVE analysis is changed to a single 3D element (C3D8), and the presented porous plasticity model is used as the material model for the analysis. All of the boundary conditions are the same as described in the RVE analysis in Chapter 3. Therefore, both the RVE study and the present model were solved under the same conditions. Note that smaller step sizes are used for the porous plasticity model compared to the RVE analysis in order to obtain convergent solutions. Step size is 10^{-4} for $T = 1$ and below, 10^{-5} for $T = 2$ and 3 with a total simulation time of $t_{total} = 1$. Moreover, the initial results from the porous model do not include any coalescence criteria. Its incorporation will be discussed in a separate section.

Figures 4.10a and 4.11a show the equivalent stress-strain relations obtained from both the RVE computations and the porous plasticity model for $f_0 = 0.01$ and $f_0 = 0.001$ for the whole T range. The model can only capture the general trend of the decrease in ductility and equivalent stress with increasing stress triaxiality. It can also be said that the porous model has better prediction in terms of equivalent stress-strain response at higher initial porosity. At $T = 1$, predictions of the model is closest to the RVE results compared to the other T values. As the stress triaxiality increases, the model overpredicts the reduction in the equivalent stress response compared to the RVE, and the opposite happens at $T < 1$. Similar conclusions can be made with the porosity evolution in Figures 4.10b and 4.11b. The model again underpredicts void growth at $T > 1$ and overpredicts at $T < 1$. Note that the model only predicts the damage due to void growth; thus, the results should be compared up the onset of void coalescence, especially at $T \approx 1$, where the shift to the uniaxial straining mode is sudden.

The studies in [57], [82] and the original study of Cocks [1] show that this formulation can approximate the yield surface of a porous body at high porosity levels such as $f = 0.05 - 0.15$, and it is discussed in [57] that the Cocks yield potential is accurate at $f = 0.01$ for $T < 2$. Although these studies are based on the yield surface only and

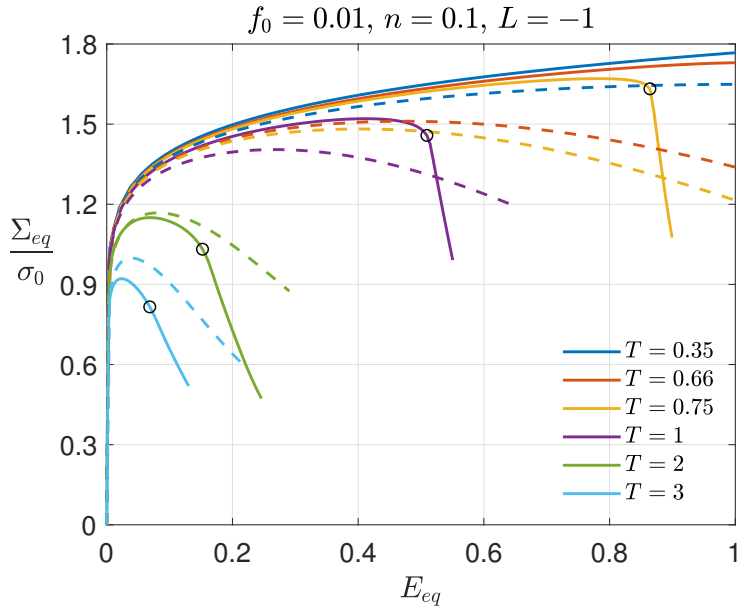

(a)

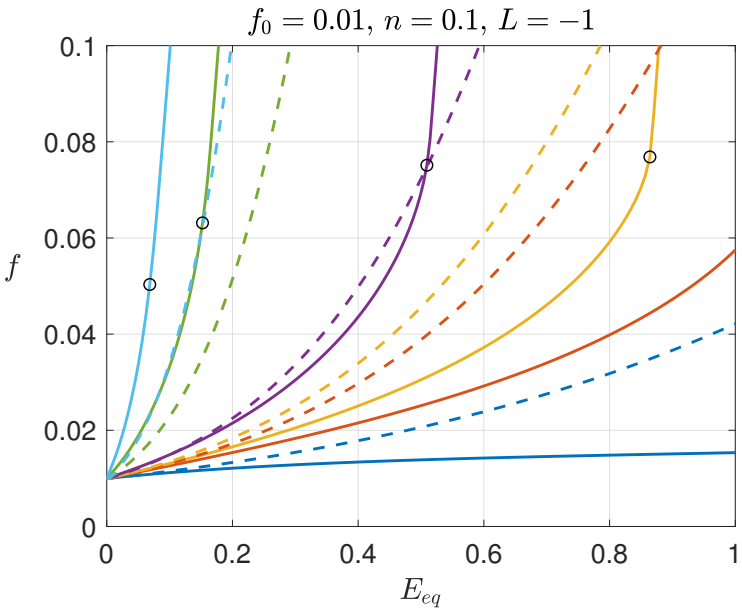

(b)

RVE Porous model

Figure 4.10: Comparison of RVE simulations (solid lines) and the porous plasticity model (dashed lines) for $f_0 = 0.01$. (a) Normalized equivalent stress-strain relation, (b) void volume fraction, f, vs equivalent strain. The onset of uniaxial straining mode is marked by $\circ$.

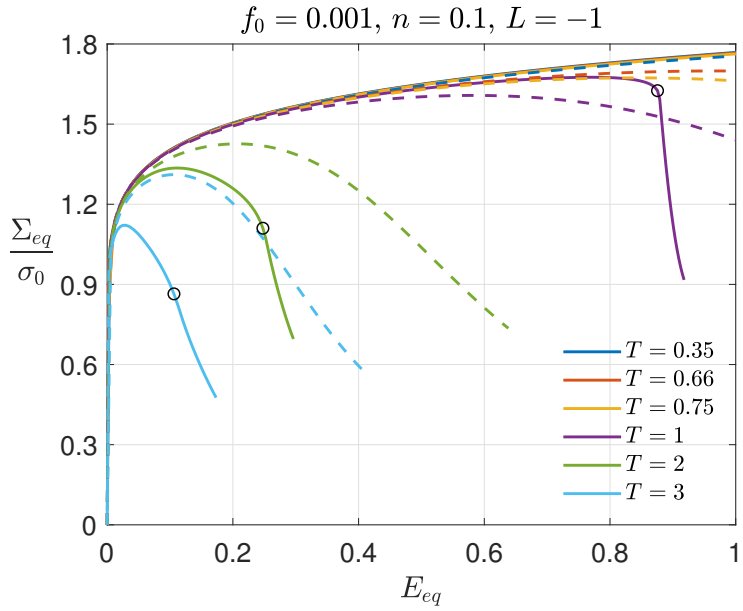

(a)

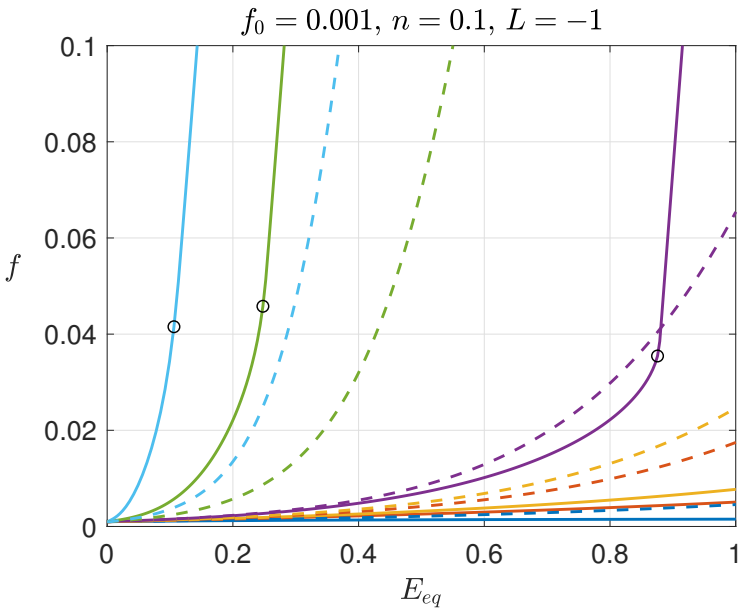

(b)

RVE Porous model

Figure 4.11: Comparison of RVE simulations (solid lines) and the porous plasticity model (dashed lines) for $f_0 = 0.001$. (a) Normalized equivalent stress-strain relation, (b) void volume fraction, f, vs equivalent strain. The onset of uniaxial straining mode is marked by $\circ$.

do not include the whole constitutive model and a material subroutine as done here, they also indicate the model's predictions are accurate at a limited T and f values. If the previous works are considered, it can be said that the model has the potential to perform better at $f > 0.05$, but such high f_0 values are not typically observed in ductile metals; thus, they are not in the scope of this study.

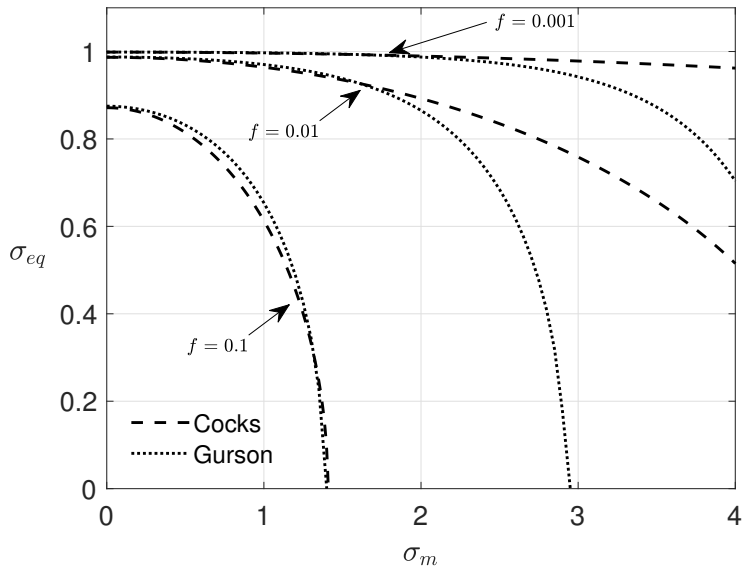

Figure 4.12: Yield surface comparison between the Cocks model and the Gurson model with parameters suggested in [38] ($q_1 = 1.25$, $q_2 = 1$, $q_3 = q_1^2$).

The reason behind the difference between the porous plasticity model and RVE simulations is twofold: (i) It is assumed that the initial spherical shape of the voids does not change during the deformation in the limit analysis of Cocks [1]. However, it is known that the voids evolve into an oblate shape at $T > 2$ and prolate shape at $1/3 < T < 1$ (examples are shown in Figure 4.9, also see [38,83]). The effect of void shape on the stress-strain response and void evolution has also been covered in the literature (see [44, 63]), which is not incorporated in the model of Cocks [1]. Similar to the GTN model, the current model cannot predict the shape change of voids under low stress triaxiality and predict higher growth. (ii) In [1], Cocks intended to build a model that is simple and compact. The resultant yield potential in Eq. (2.1) describes an ellipse in σ_m - σ_{eq} space at every porosity level. However, it has been shown in [34] that the elliptic shape is only suitable for a limited porosity range ($f > 0.05$). The differences in the yield surface of Cocks and Gurson is visualized in Figure 4.12.

Surfaces match closely at $f = 0.1$, but as the porosity decreases, the current model predicts a higher yield point compared to the Gurson model, especially at greater σ_m regions. Knowing that the Gurson model can closely match the RVE simulation results at high stress triaxiality (see [38]), it is no surprise that the current model cannot predict the void growth and damage at such T values. Moreover, since both Gurson and Cocks models yield similar values at lower T regions, they both suffer from the assumption of spherical void growth.

4.5 Extension of the porous plasticity model

In order to obtain a better correspondence between the porous plasticity model and RVE simulations and also to have a model that can be fitted to different material responses, an extension with two constant fitting parameters is proposed. A constant fitting parameter, a_1, is added to the yield function, as

$$\phi = \sqrt{\frac{\sigma_{eq}^2}{g_1(f_{eff})} + \frac{\sigma_m^2}{a_1\, g_2(f_{eff})}} - \sigma_y \tag{4.3}$$

with the same g functions as [1]. Additionally, an effective porosity evolution, $\dot{f}_{eff}$, is proposed which consists stress triaxiality, T, and another parameter, a_2, as

$$\dot{f}_{eff} = \dot{f}\, T^{a_2} = \dot{\varepsilon}_v^p (1-f) T^{a_2}. \tag{4.4}$$

T in Eq. (4.4) acts as a triaxiality scaling factor. For $T > 1$, the void growth is amplified with the increasing T, and below $T = 1$, the triaxiality's effect on growth is reduced. a_2 is used for adjusting the level of effect of T on the void growth. Note that it is not possible to obtain better predictions only by adjusting the porosity functions due to the shape of the yield function. Therefore, a change in porosity evolution is suggested in addition to the fitting parameter in the yield function. This approach solves the problems with void shape change in lower T regions by lowering the effective growth of the voids while also addressing the problems at the high T regime originated from the simple description of the yield potential. However, the effective porosity of the extended model should be treated as a *damage variable* rather than the physical volume of the voids with the current addition. Fitting parameters are selected by trial and error based on the fit of the pore evolution of the model and RVE results, as $a_1 = 1.05$, $a_2 = 0.9$ for $n = 0.1$ and $a_1 = 1.2$, $a_2 = 0.9$ for $n = 0.2$. Also, since T may not be constant during any deformation process, it is calculated in the material subroutine (UMAT) and used in the pore evolution rule at each solution increment. Note that the extension of the model is based on RVE simulations at $T > 0.33$. For lower triaxialities than 0.33, additional studies are required. For the current implementation, the original porosity evolution equation without T and a_2 is used at $T < 0.33$.

In Figures 4.13, 4.14 and 4.15, extended porous plasticity model predictions are plotted against RVE simulations results for the whole T range at two different initial

porosity levels and hardening exponents. Normalized equivalent stress versus equivalent strain results are shown in Figures 4.13a, 4.14a and 4.15a. There is a substantial improvement in the fit with RVE simulation data and the porous plasticity model for the whole stress triaxiality range. Predictions of the model are slightly better for small initial pore fraction $f_0 = 0.001$ at both hardening exponents. Also, the model is able to capture the void growth and sudden decrease in the stress after the void coalescence at $T \approx 3$, but as the T drops, the shift to the coalescence mode is sudden and cannot be predicted with the void growth model only. Similar improvements can also be observed for the pore evolution in Figures 4.13b, 4.14b and 4.15b. Here, the extended model is fitted to the two different hardening exponents using only the parameter a_1 (see Figures 4.14b and 4.15b). It should be noted that the modification for the model is solely mathematical and does not depend on any mechanical study. However, it provides significantly better results while keeping the simple description of the model and has a highly flexible framework for calibration to different ductile porous materials. Moreover, using different fitting parameters at different f_0 can further improve the model's performance. In the following section, the extended model is compared with the GTN model.

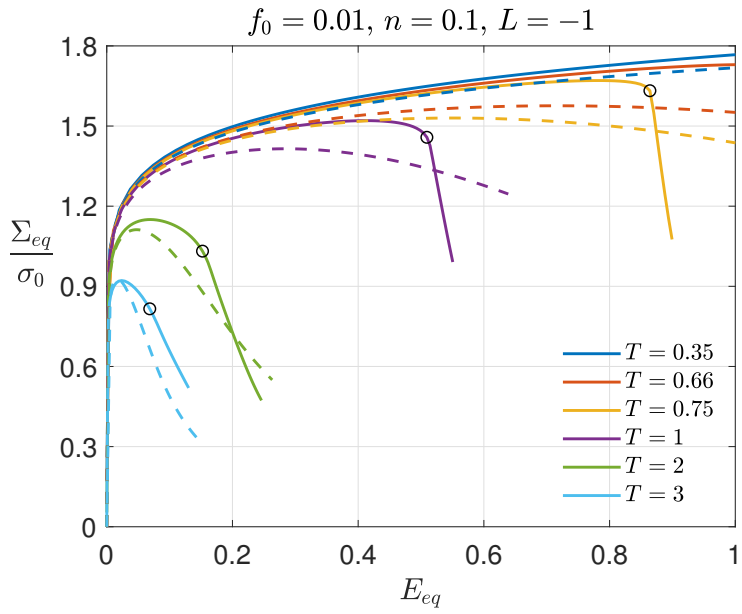

(a)

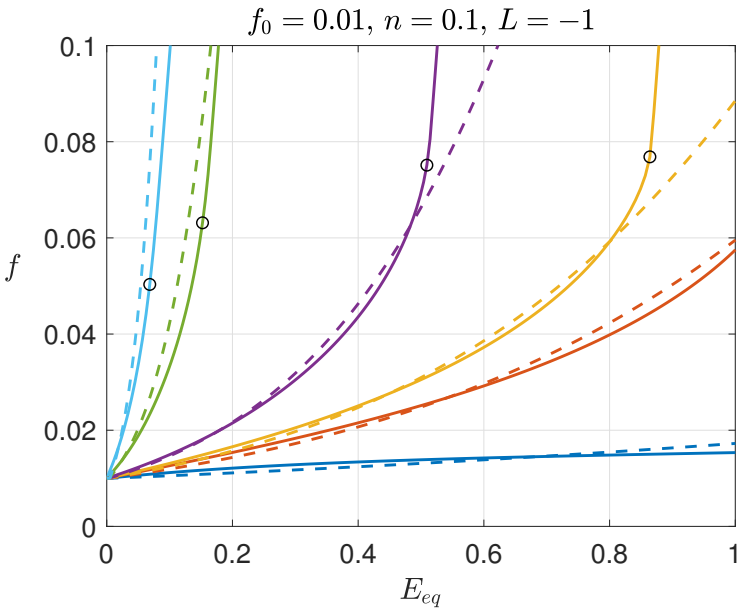

(b)

RVE Porous model

Figure 4.13: Comparison of RVE simulations (solid lines) and the porous plasticity model (dashed lines) for initial porosities for $f_0 = 0.01$ and $n = 0.1$. (a) Normalized equivalent stress-strain relation, (b) void volume fraction, f, vs equivalent strain. Fitting parameters: $a_1 = 1.05$ $a_2 = 0.9$. The onset of uniaxial straining mode is marked by $\circ$.

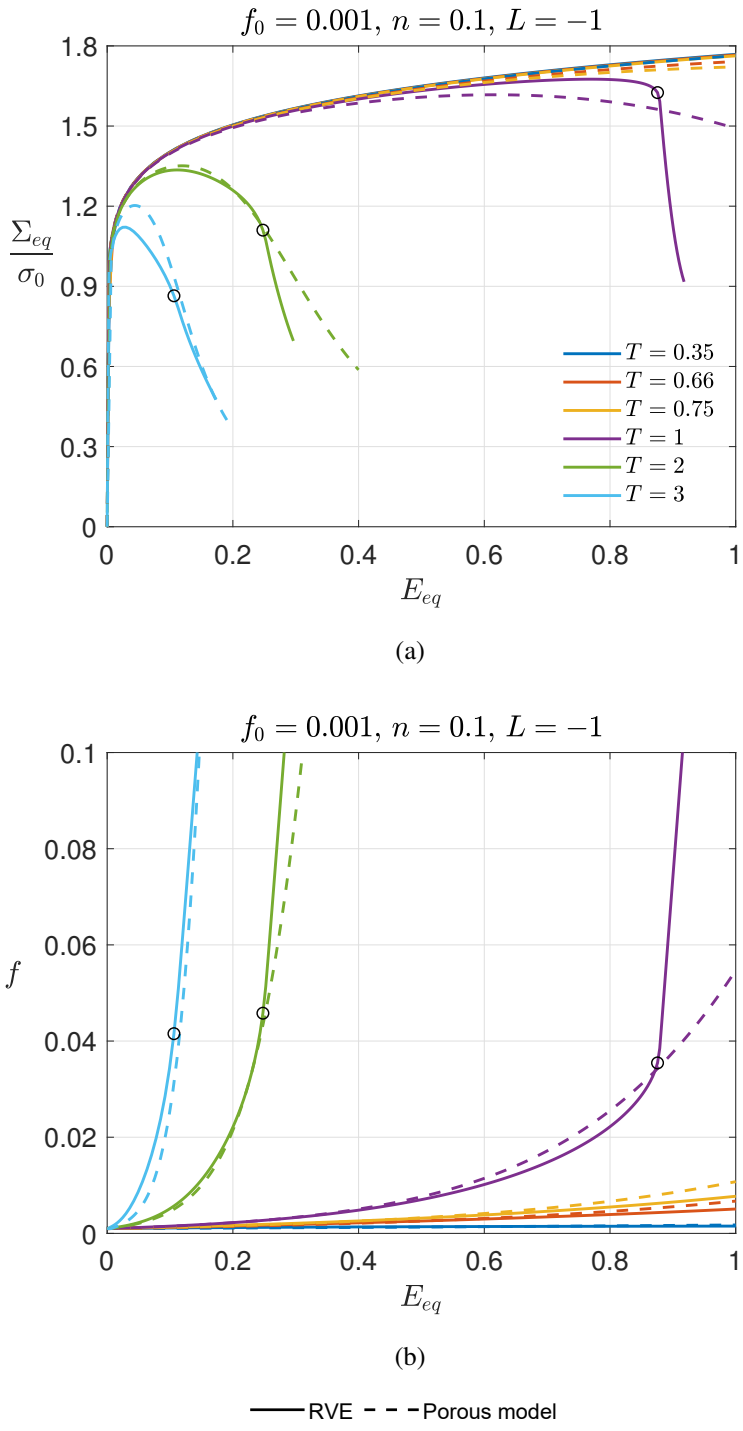

Figure 4.14: Comparison of RVE simulations (solid lines) and the porous plasticity model (dashed lines) for initial porosities for $f_0 = 0.001$ and $n = 0.1$. (a) Normalized equivalent stress-strain relation, (b) void volume fraction, f, vs equivalent strain. Fitting parameters: $a_1 = 1.05$ $a_2 = 0.9$. The onset of uniaxial straining mode is marked by $\circ$.

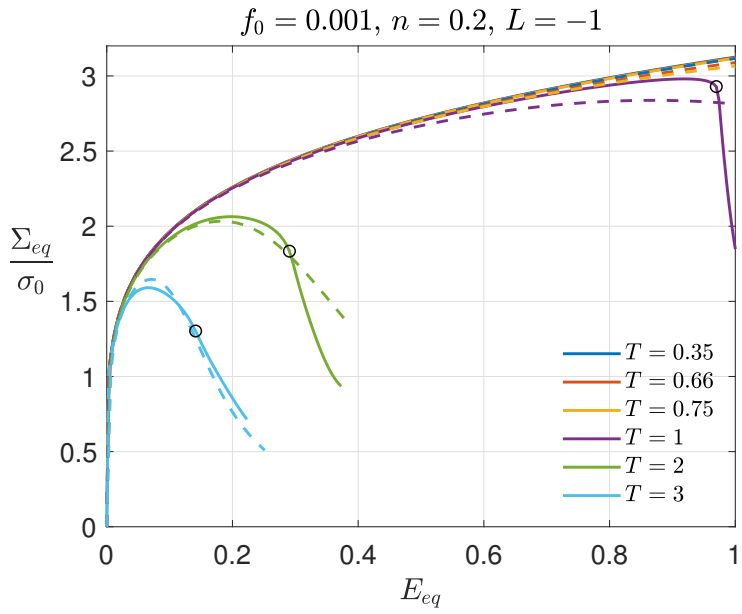

(a)

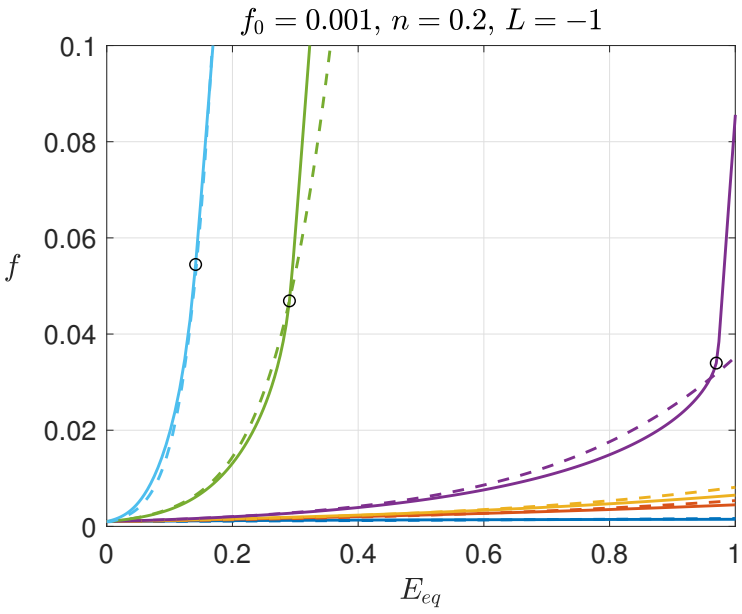

(b)

RVE Porous model

Figure 4.15: Comparison of RVE simulations (solid lines) and the porous plasticity model (dashed lines) for initial porosities for $f_0 = 0.001$ and $n = 0.2$. (a) Normalized equivalent stress-strain relation, (b) void volume fraction, f, vs equivalent strain. Fitting parameters: $a_1 = 1.2$ $a_2 = 0.9$. The onset of uniaxial straining mode is marked by $\circ$.

4.6 Comparison of the GTN model and the extended porous plasticity model

In this section, the GTN model and the extended porous plasticity model will be compared with respect to RVE calculations. The yield function of the GTN model is

$$\phi = \frac{\sigma_{eq}}{\sigma_y} + 2q_1 f cosh(\frac{3q_2\sigma_m}{2\sigma_y}) - (1 + q_3 f^2) \tag{4.5}$$

where σ_{eq} is the von Mises equivalent stress, σ_m is the mean stress, σ_y is the yield stress, q_1 and q_2 are the fitting parameters introduced in [36] with $q_3 = q_1^2$. Void growth is governed by

$$\dot{f} = (1 - f)tr(\dot{\boldsymbol{\varepsilon}}^p). \tag{4.6}$$

Simulations are performed with the GTN model, which is implemented in commercial software Abaqus as a porous metal plasticity model (refer to [74, 84] for the details of the GTN model and the numerical implementation). Fitting parameters suggested in [38] are used ($q_1 = 1.25$, $q_2 = 1$ and $q_3 = q_1^2$), which are obtained based on the fit of the GTN model and the RVE study conducted with axisymmetric elements. The RVE study in [38] is conducted with similar initial porosity values ($f_0 = 0.0013$ and $f_0 = 0.0104$) and using the same hardening conditions.

Results with the GTN model are obtained using the same method as the porous plasticity model. A single hexahedral element is solved under constant triaxial stress employing the same procedure as the RVE simulations. The voided finite element model in the RVE study is changed to a single hexahedral element, and the boundary conditions are applied in the same way.

In Figures 4.16 and 4.17, predictions of the extended model and the GTN model are plotted with RVE simulation results for the whole T range at $f_0 = 0.01$ and $f_0 = 0.001$. Figures 4.16a and 4.17a illustrate the equivalent stress-strain responses of the models. Both models yield comparable results compared to the RVE simulations until the onset of coalescence. The GTN model is slightly more accurate at $T > 1$, while the present porous plasticity model can give better predictions at $T < 1$. Models show a gradual decrease in the equivalent stress at moderate triaxiality values, $T \approx 1$. However, RVE analysis indicates that the damage due to void growth has a smaller effect of stress-strain response up to the onset of coalescence. Since the phenomenological models are derived based on a spherical pore shape, both models

gradually decrease the stress with the increasing porosity. In the RVE analysis, the void shape changes significantly at such T values that decrease the effect of void growth on stress carrying capacity.

The evolution of void volume fraction f with respect to the equivalent strain is plotted in Figures 4.16b and 4.17b. It can be seen that, at $f_0 = 0.001$, both models can closely predict the behavior of the RVE at all T values up to void coalescence. However, at $f_0 = 0.01$ and $T < 1$, predictions of the extended porous model are clearly more accurate compared to the GTN model. Moreover, the GTN model has better accuracy for the void evolution at $T > 1$ and $f_0 = 0.01$, while the extended model is overpredicting slightly. It can be said that the parameters identified by Koplik and Needleman [38] for the GTN model works well compared to the current RVE analysis, specifically at $T > 1$. Moreover, for q_1 and q_2, additional parameters are examined ($q_1 = 1.2 - 1.3$ and $q_2 = 0.95 - 1.05$) by trial and error to find a more suitable parameter set. Improvements can be obtained in equivalent stress-strain response with $q_2 = 1.2$ and $q_2 = 1$. In terms of porosity evolution, closest results are obtained with the $q_1 = 1.25$ and $q_2 = 1$. The overall predictions of the GTN model are found to be highly successful at $T > 1$. As T decreased, the GTN model overpredicts the void growth in the given parameter range. In the current work, the common form of the GTN model is used but note that there are extensions of the GTN model, such as the GLD model, that improve the response of the model at low T values.

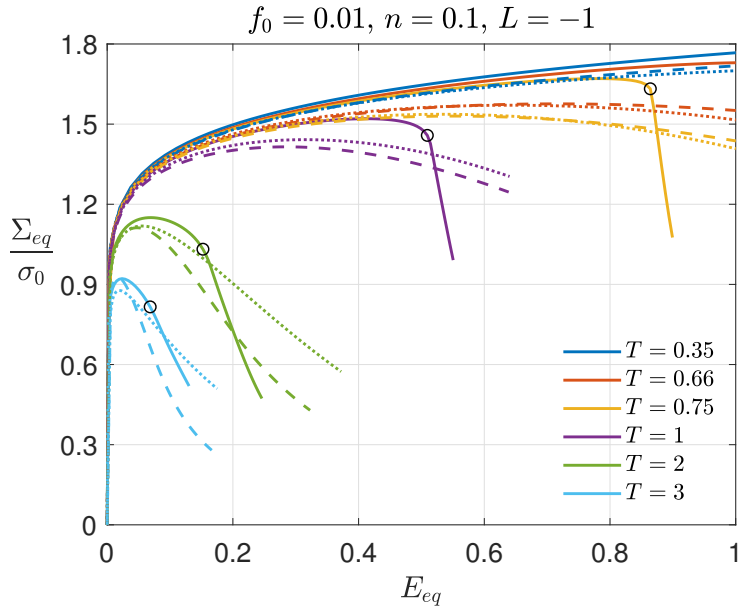

(a)

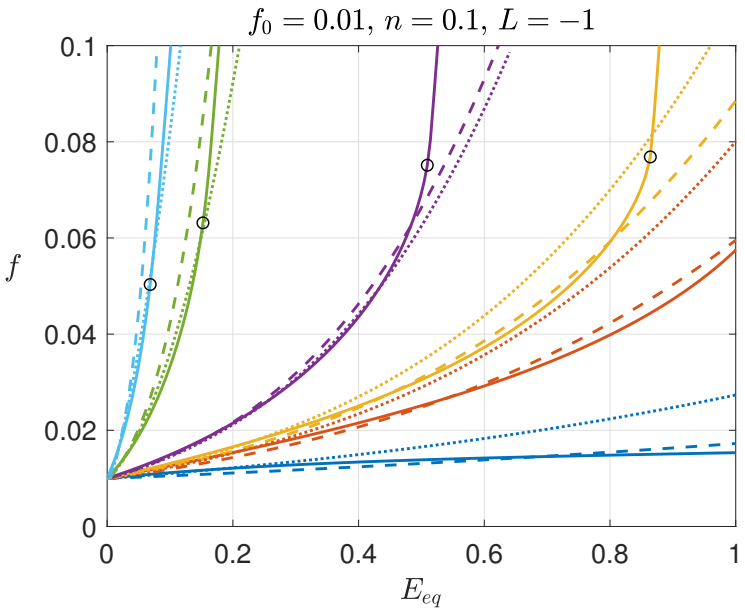

(b)

RVE Porous model GTN model

Figure 4.16: Comparison of the extended porous plasticity model (dashed lines) and the GTN model (dotted lines) together with RVE simulations (solid lines) for initial porosities for $f_0 = 0.01$. (a) Normalized equivalent stress-strain relation, (b) void volume fraction, f, vs equivalent strain. Fitting parameters: $a_1 = 1.05$ $a_2 = 0.9$ for the extended porous plasticity model and $q_1 = 1.25$ $q_2 = 1$ for the GTN model. The onset of uniaxial straining mode is marked by $\circ$.

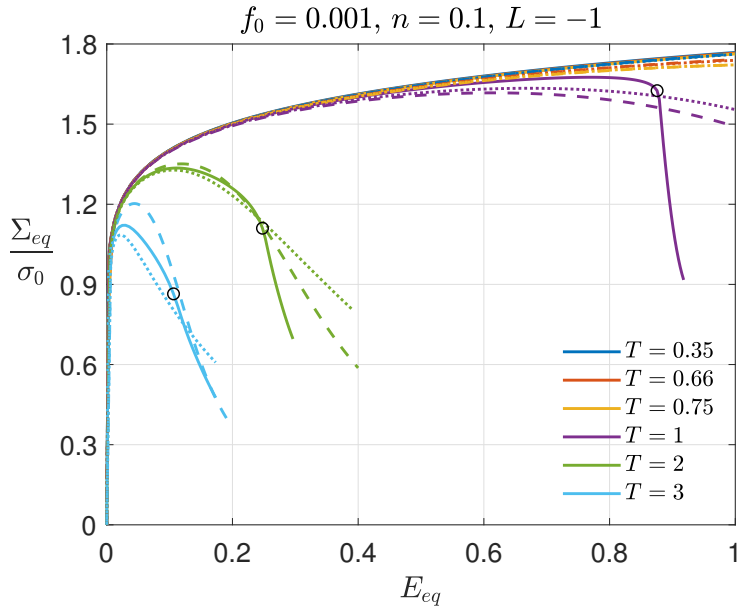

(a)

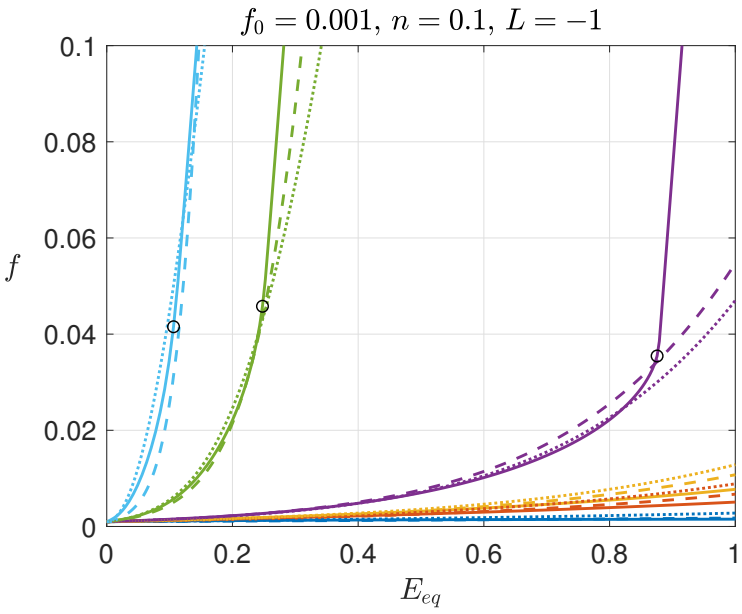

(b)

RVE Porous model GTN model

Figure 4.17: Comparison of the extended porous plasticity model (dashed lines) and the GTN model (dotted lines) together with RVE simulations (solid lines) for initial porosities for $f_0 = 0.001$. (a) Normalized equivalent stress-strain relation, (b) void volume fraction, f, vs equivalent strain. Fitting parameters: $a_1 = 1.05$ $a_2 = 0.9$ for the extended porous plasticity model and $q_1 = 1.25$ $q_2 = 1$ for the GTN model. The onset of uniaxial straining mode is marked by $\circ$.

4.7 Extended porous plasticity model coupled with void coalescence

Void coalescence is known to be the final phase of the failure for ductile porous metals. Although there are many detailed coalescence models proposed in the literature (see e.g. [63, 85–87] and a unified growth and coalescence model [88]), the simple phenomenological approach in [41] is adopted to couple the porous induced damage model with void coalescence. The coalescence model utilizes an effective porosity, denoted by $f^\star$, to artificially accelerate the void growth after a critical porosity level. Therefore $f^\star$ is used in the porosity functions of the coupled model as follows:

$$\phi = \sqrt{\frac{\sigma_{eq}^2}{g_1(f^\star)} + \frac{\sigma_m^2}{a_1\, g_2(f^\star)}} - \sigma_y \tag{4.7}$$

and

$$f^\star = \begin{cases} f_{eff} & \text{if } f_{eff} \leq f_c \\ f_c + \kappa(f_{eff} - f_c) & \text{if } f_{eff} > f_c \end{cases} \tag{4.8}$$

with κ being a fitting parameter that determines the level of acceleration, and f_c is the critical porosity. Following the work in [38], κ and f_c are selected to match the porosity vs. effective strain curves of the model and RVE analysis. Results are shown in Figure 4.18 for the high T region, where the coalescence can be observed in the given equivalent strain range. The acceleration of the void growth accompanied by a sudden decrease of the equivalent stress is observed similar to the GTN model. Notice that the critical porosity value is similar to the one used in [38]; however, a relatively higher κ value is used to obtain similar results with the current model.

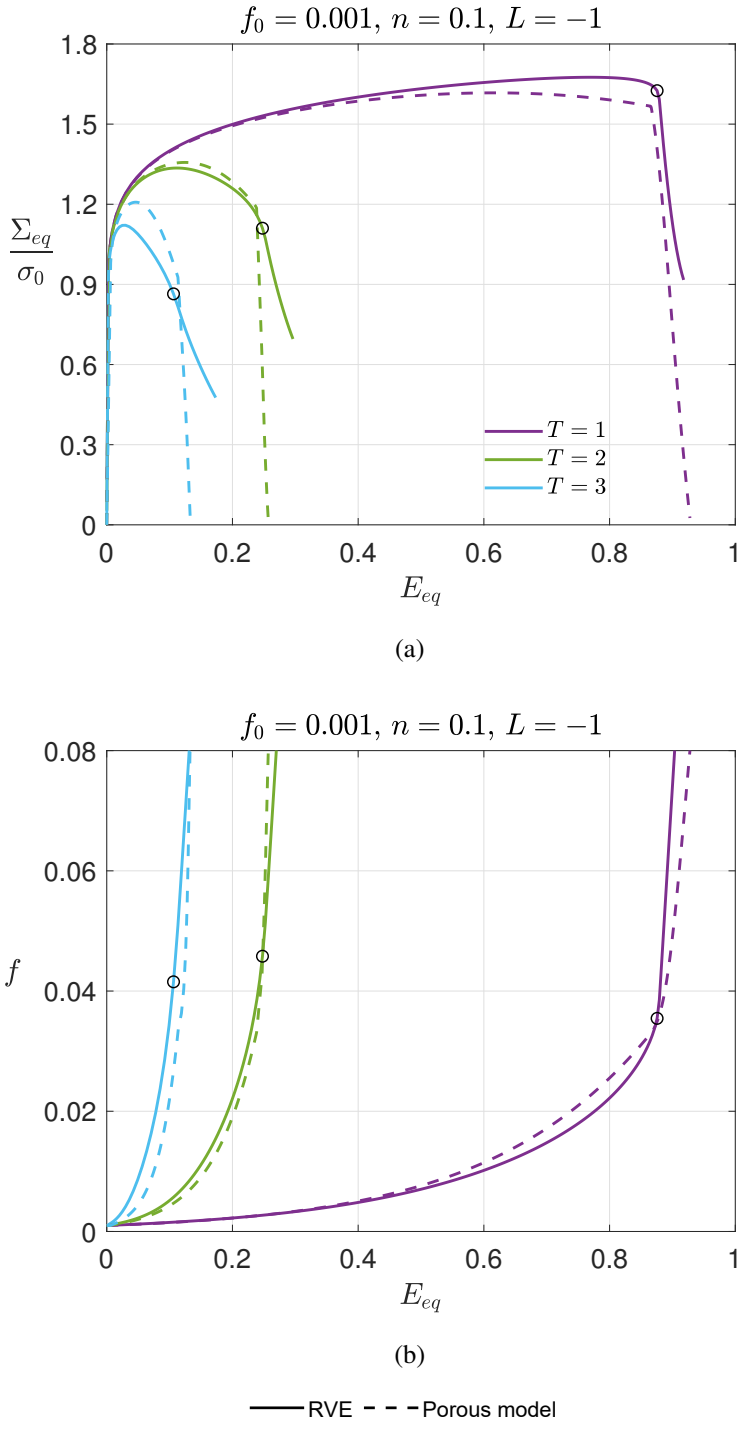

Figure 4.18: Comparison of RVE and the extended porous plasticity model with coalescence for $f_0 = 0.001$, $f_c = 0.033$ and $\kappa = 20$. (a) Normalized equivalent stress-strain relation, (b) void volume fraction, f, vs equivalent strain. Fitting parameters: $a_1 = 1.05$ $a_2 = 0.9$. The onset of uniaxial straining mode is marked by $\circ$.

4.8 Uniaxial tension simulations on blunt notched and smooth specimens

This section covers the application of the current porous plasticity framework to tensile ductile fracture simulations. Three different specimen types are used, one with a smooth section and two with blunt circular notches in the center, as shown in Figure 4.19. Only the 1/8 portion is modeled and solved in the finite element software (see Figure 4.21) using the symmetry boundary conditions. The notched specimens are modeled based on the work in [89]; thus, the smallest circular area at the center are the same for the notch radiuses of 4 and 8 mm. The center of the circular notch is in line with the outer surface of the specimen for the 8 mm notch radius, while the 4 mm radius notch center is 4 mm inside the outer surface to have the same initial area at the center of the specimen. The smooth specimen is created with a 5 mm circular fillet radius. The fillet starts at 10 mm from the left side, and the fillet center is aligned with the edge. Material parameters given in Table 4.1 are used with hardening exponent, $n = 0.1$, and initial porosity, $f_0 = 0.001$.

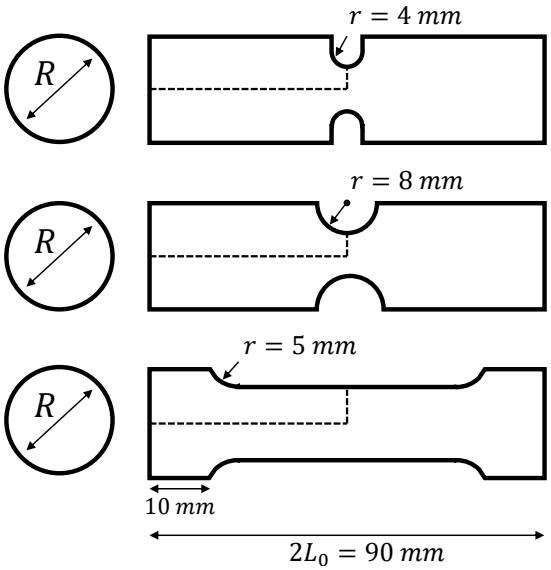

Figure 4.19: Smooth and notched tensile test specimen geometry. Notch radius $r = 4$ and 8 mm, specimen diameter $R = 40$ mm, length $2L_0 = 90$ mm, and smooth specimen fillet radius $r = 5$ mm.

Simulations are performed through 3 different damage and fracture models for each

specimen. Two of them are the coupled ductile damage and fracture models, which are the GTN model of Abaqus and the porous plasticity model presented in the thesis with the extensions. The third one is the uncoupled Johnson-Cook fracture model [25]. Here, the uncoupled model means that the damage does not have an impact on the constitutive equations. The Johnson-Cook model utilizes a stress triaxiality and equivalent plastic strain based equation to calculate the damage parameter with the following equation:

$$\varepsilon^f = D_1 + D_2 exp(D_3 T) \tag{4.9}$$

where D_1, D_2 and D_3 are the material parameters, ε^f is the equivalent strain to fracture, T is the stress triaxiality. Note that the Johnson-Cook damage model has two additional terms that bring the effects of strain rate and temperature. These terms are not used because both the GTN and the present porous plasticity model are rate and temperature independent.

The evolution of the damage is given by

$$D = \sum \frac{\Delta \bar{\varepsilon}^p}{\varepsilon^f} \tag{4.10}$$

where $\Delta \bar{\varepsilon}^p$ is the incremental equivalent plastic strain. Then, the fracture is said to occur at $D = 1$. This is a built-in ductile fracture model in Abaqus with the name of the Johnson-Cook damage initiation model. In Abaqus terminology, the initiation and the evolution of damage is slightly different than the conventional use. In Abaqus, when the damage parameter, D, reaches a value of 1, it is considered that the damage has initiated in that element and requires the user to input a damage evolution rule to trigger element deletion and predict fracture. Therefore, the evolution of damage corresponds to the part after $D = 1$. For the current analysis in Abaqus, the displacement type damage evolution is used and 'displacement at failure' value is chosen as 0 in order to delete the elements that reach $D = 1$. J2 plasticity model is used as the constitutive model for the Johnson-Cook fracture simulations.

The model parameters D_1, D_2 and D_3 are obtained from the RVE simulations at $f_0 = 0.001$. To obtain a better fit between the Johnson-Cook model and RVE results, RVE is solved for additional stress triaxiality values. The values chosen for T are 1, 1.2, 1.4, 1.6 ,1.8 ,2 ,2.5 and 3. For the values lower than $T = 1$, the coalescence did not occur even at large strain values; thus, they are not included. The fracture strain

value is taken at the onset of coalescence, and the results are shown in Figure 4.20. D parameters are obtained through curve fitting and listed in Table 4.3. Notice that there is an asymptotic behavior as T gets closer to the lower values. However, fracture loci is shown to be different under compressive or shear-tension combined loads due to the change in fracture mechanisms (see e.g. [18, 90–92]); thus, the current fracture loci is valid only at $T > 0.33$.

The fitting parameters of the GTN model and the porous plasticity model are shown in Table 4.3. a_1 is taken as 1.17 to match the present porous model and the GTN model results in the notched tensile tests. The critical pore fraction, f_c, the pore fraction at failure, f_f, and κ. f_f is utilized in the Abaqus GTN model as an indication of complete element failure, and it is used to calculate the κ. To have a comparable behavior after the onset of void coalescence, the same κ and f_f values are implemented in the porous plasticity model, and elements that reach $f = f_f$ are deleted from the finite element mesh. f_c value is obtained from the RVE analysis. Note that void nucleation is disregarded for both coupled damage models.

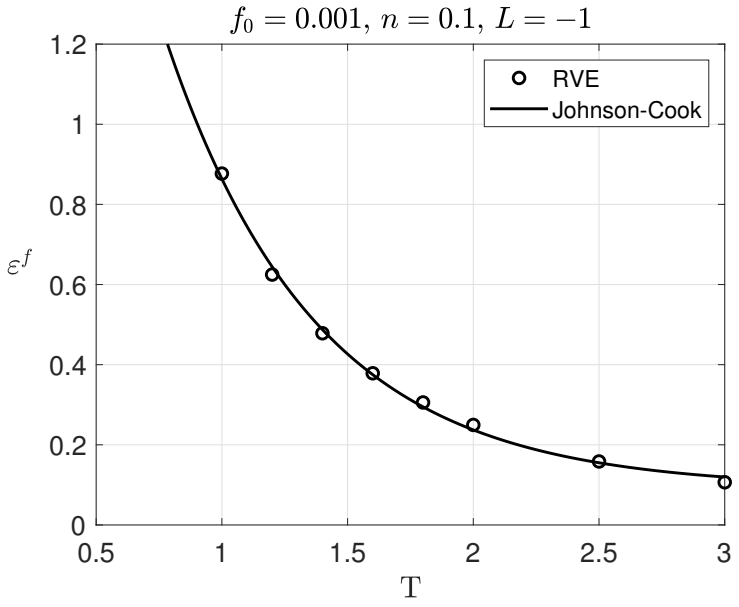

Figure 4.20: Fracture loci of the Johnson-Cook model based on the RVE simulations for $f_0 = 0.001$ and $n = 0.1$.

The explicit solver of Abaqus is used for the tension simulations with 3D elements and reduced integration (C3D8R of Abaqus). The total number of elements for the

Table 4.3: Model and material parameters for the tensile simulations

Elasticity and J2 plasticity					
E/σ_0	n	E [MPa]	ν		
300	0.1	70000	0.3		
Current porous plasticity model					
a_1	a_2	f_0	f_c	κ	f_f
1.17	0.9	0.001	0.033	4.593	0.2
GTN model ($q_3 = q_1^2$)					
q_1	q_2	f_0	f_c	κ	f_f
1.25	1	0.001	0.033	4.593	0.2
Johnson-Cook model					
D_1	D_2	D_3			
0.0925	4.817	-1.673			

smooth and notched specimens with $r = 4$ & $r = 8$ are 55132, 34755 and 38301, respectively. Mesh density is increased at the lower portion of the notched and the smooth specimens in the direction of the tensile load, as shown in Figure 4.21. The idea here is to have a mesh with reasonable aspect ratios at the later stages of the deformation because elements in the critical regions tend to elongate in the tensile loading direction. Similar meshing strategies are used in [93] for round bars and plane strain specimens. The material density is taken as $2.7\ g/cm^3$, which is a typical density value for aluminum. In order to obtain a quasi-static analysis with the explicit solver, mass scaling is utilized with a target time increment of 10^{-6}. The total time for the simulation is 1. Comparing the internal and kinetic energy of the finite element model during the simulation is a common practice to ensure a quasi-static solution. Abaqus recommends that the kinetic energy (ALLKE) should be 5-10% of the internal energy (ALLIE) of the model (see [74] Energy balance). In the present simulation with mass scaling, the kinetic energy is found to be between $0.1 - 0.001\%$ of the internal energy throughout the simulations for every specimen and modeling approach.

Explicit simulations require the explicit versions of the user material and hardening

(a) Smooth (b) $r = 4$ mm (c) $r = 8$ mm

Figure 4.21: Finite element models of the smooth and notched tension specimens.

subroutines (VUMAT and VUHARD). The implementation of the porous plasticity model is not specifically addressed for VUMAT in the implementation chapter because the implementation can be done for both types of subroutines, and conversion from UMAT to VUMAT is a straightforward procedure for the given porous plasticity model. However, the main differences between UMAT and VUMAT will be stated here briefly. Firstly, an explicit finite element solution does not require a tangent modulus from the subroutine. The rotation of the tensorial variables is not required. The order of the shear components in Voigt notation of stress and strain is different. For UMAT, the order is 12, 13, and 23; however, for VUMAT, the order changes to 12, 23, and 13. Another difference is that the shear strain components are not stored as engineering strains for the VUMAT subroutine. Moreover, VUHARD, which is used to perform simulations with the desired strain hardening equation, is basically the same as UHARD subroutine with some differences in the name of the variables inside the subroutine (Refer to [74], User subroutine reference guide for the details of the user subroutines). Note that name differences are also present for UMAT and VUMAT subroutines.

The results from the tension simulations are shown in Figure 4.22. In Figure 4.22a, engineering stress-strain response is demonstrated. Stress is normalized with the initial yield stress, σ_0, and the initial area of the top surface, $A_0 = \pi(R/2)^2/4$. It is clear

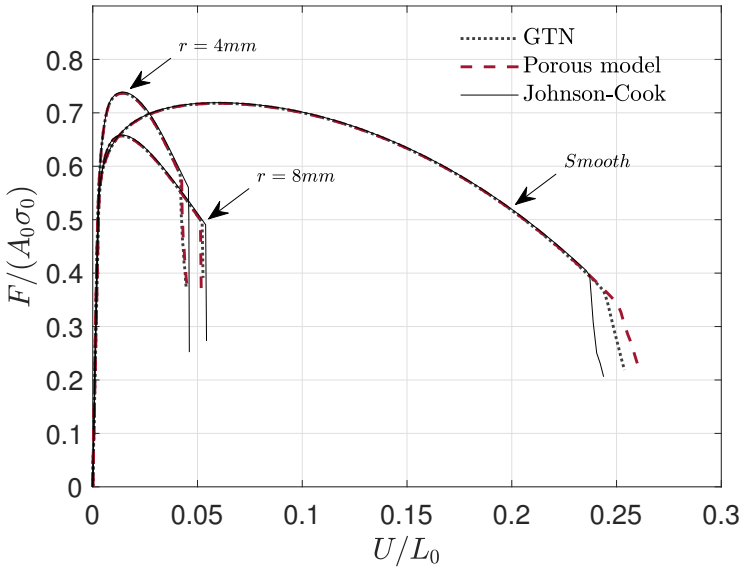

(a)

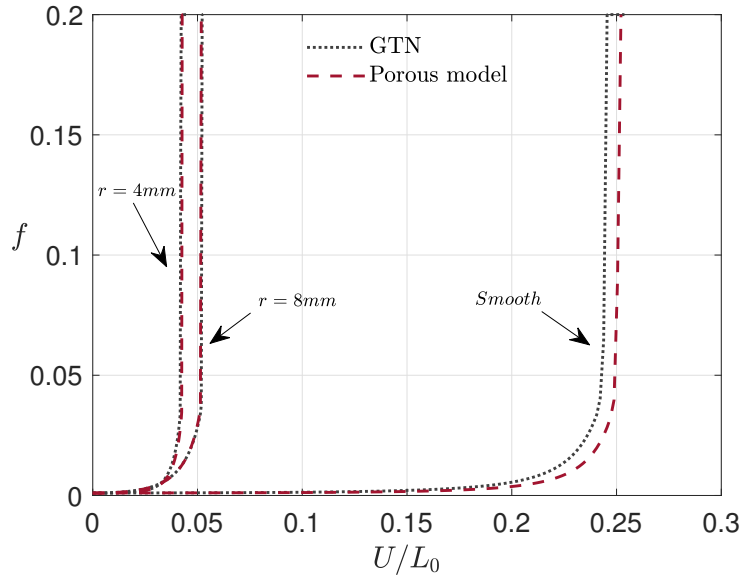

(b)

Figure 4.22: Tensile simulation results for 3 different specimens. (a) Normalized eng. stress vs. eng. strain, (b) evolution of porosity at the critical element.

that all of the models predict similar tensile stresses and fracture points. The coupled models yield slightly lower stresses in each case as a result of porosity induced damage. In the notched specimens, both the GTN and the present porous model produce almost identical solutions while the Johnson-Cook model predicts fracture at a higher

strain value. The biggest difference occurs in the smooth specimen. The porous plasticity model anticipates the latest fracture point compared to GTN and Johnson-Cook models. Another observation here is that the notched specimens show a sudden drop in the stress indicating a faster crack propagation while the smooth specimen fails relatively slowly. Additionally, the Johnson-Cook model yields the most conservative result only for the smooth specimen.

In Figure 4.22b, the evolution of the void volume fraction, f, is shown for the coupled models. The value is taken from the element at the center of the model where the crack initiates for all three specimens. The results are in line with the stress-strain relations, where the predictions for the notched specimens are almost identical and the GTN model predicts a higher void growth which results in a smaller fracture strain than the porous plasticity model.

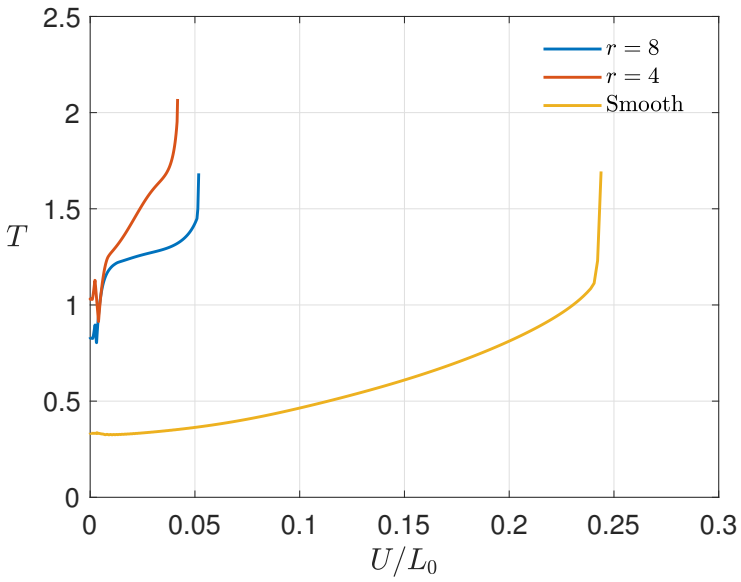

Figure 4.23: Evolution of the stress triaxiality at the critical element.

The stress triaxiality evolution is demonstrated in Figure 4.23. Again data are taken from the critical element, which is the element that fails first. The results show that the stress triaxiality starts at around 0.8 and 1 for the notched specimens with $r = 8$ and $r = 4$, respectively. As the notch radius gets smaller, stress triaxiality increases in the center of the specimen. Also, with a smaller notch radius, T reaches even higher values before the fracture point. Moreover, the specimen with a smooth section is

under a homogeneous uniaxial deformation state initially ($T = 1/3$). The increase in the macroscopic deformation results in strain localization and necking in the middle section. Consequently, T gradually increases and reaches a value slightly higher than 1 just before the fracture. The final sudden increase in the T corresponds to the deformation after the onset of void coalescence which might not correspond to physical phenomena.

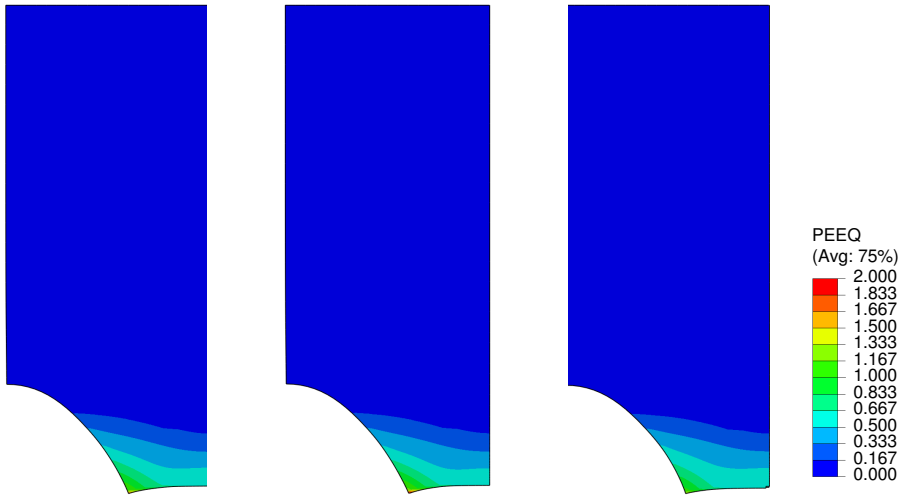

(a) GTN (b) Porous model (c) Johnson-Cook

Figure 4.24: Final fracture shapes and the equivalent plastic strain distribution for the notched specimen with $r = 8$ mm.

In Figures 4.24, 4.25 and 4.26, the final fracture shapes of the notched and the smooth specimens are shown together with the equivalent plastic strain distribution. All three models show a cup-shaped fracture surface where the crack initiates in the center and propagates outwards horizontally. It should be noted that the specimen with a smaller notch radius has a relatively horizontal fracture surface than others. The equivalent plastic strain distributions are highly similar for the notched specimens. The most significant difference again is seen in the smooth specimen where the porous model showed a higher plastic strain accumulation before fracture because of the larger fracture strain.

An important issue to note here is that the a_1 value of the porous plasticity model used here is larger than what is found in the RVE simulations. Having a smaller a_1

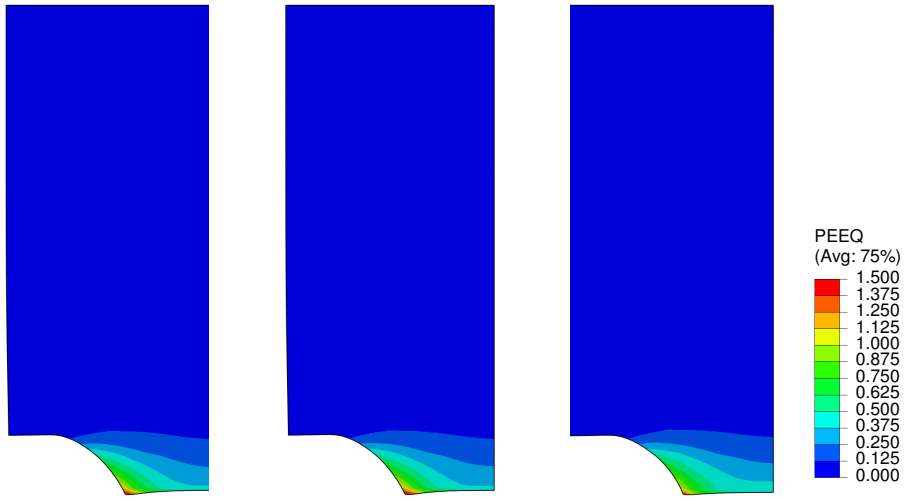

(a) GTN (b) Porous model (c) Johnson-Cook

Figure 4.25: Final fracture shapes and the equivalent plastic strain distribution for the notched specimen with $r = 4$ mm.

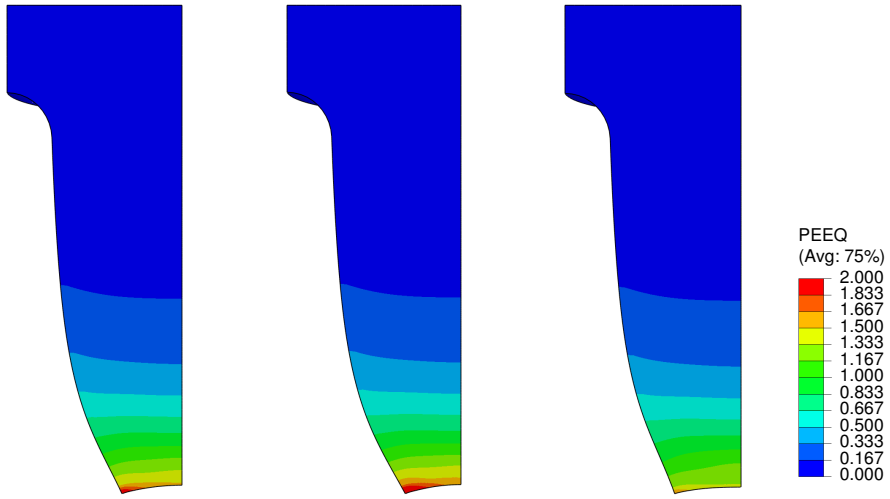

(a) GTN (b) Porous model (c) Johnson-Cook

Figure 4.26: Final fracture shapes and the equivalent plastic strain distribution for the specimen with a smooth middle section.

value results in a slower void growth for the porous model. Although a_1 was found to be 1.05 in the RVE study, here, it is used as 1.17 to closely match the GTN model and the present porous plasticity model in the notched tensile simulations. This approach

is preferred in order to show that the present model can predict similarly to the well-known GTN model. However, it is observed that at the smooth specimen, the present model predicts slower growth of porosity and a higher fracture strain compared to the GTN model. Such behavior is expected because RVE study showed that the GTN model has a tendency to over-predict the porosity evolution at lower T regions.

CHAPTER 5

CONCLUSION

This thesis covers the implementation and assessment of a rate-independent porous plasticity model based on the yield potential in [1]. The potential is formed in terms of equivalent and hydrostatic stress components and two porosity functions. The model covers only the growth of existing voids and disregards void nucleation. Assessment is done through RVE calculations under constant stress triaxiality. The model is implemented as a user material subroutine in Abaqus using a basic predictive-corrective scheme of classical J2 plasticity for the solution of constitutive equations. The consistent tangent modulus is calculated numerically with the perturbation method. RVE calculations are conducted with a displacement controlled method in a 3D setting. Comparisons are made with the well-known GTN model. An extension is proposed to the constitutive equations in order to improve the performance of the model based on the RVE analysis. Moreover, the extended model's performance is addressed through tension simulations on notched and smooth bars. Comparisons are made with the GTN model and the uncoupled Johnson-Cook fracture model. The key findings of this thesis are listed below.

- The comparison between the yield surfaces of Cocks and Gurson shows that these potentials have similar behaviors at higher porosity levels ($f \approx 0.1$). At lower porosity, they are in agreement up to high triaxiality regions. After ($T > 2$), Cocks' potential predicts a higher yield point compared to Gurson's potential.
- Results show that the initial proposition of the porous plasticity model underpredicts the yield point at high stress triaxiality regime compared to the RVE analysis, which is consistent with the yield surface differences with the GTN

model.

- Extension of the model provides significant improvements in the predictions of the model for both void growth and equivalent stress-strain relation while keeping the simple formulation.
- A simple coalescence relation is implemented to the present porous plasticity framework to predict the final failure phase of ductile damage and fracture.
- Tension simulations indicate that the extended model is able to yield identical results to the GTN model in notched specimens in terms of porosity evolution and engineering stress-strain response. The results from the smooth specimen showed that the extended model predicts slightly higher fracture strain compared to the GTN model.

The thesis presents a starting point for the development of an alternative porous plasticity model for ductile damage and fracture prediction. Although the results are convincing to some degree, there are still areas to be improved in terms of both computational and poro-mechanical aspects.

- The damage evolution related to the void growth is performed at the end of the prediction-correction scheme. Therefore, the yield function is not affected by the change in porosity in the current increment of the numerical solution. Although this problem is solved by using sufficiently small step sizes, and convergent solutions are obtained. More robust numerical solution algorithms should be implemented similar to the GTN implementations.
- The current work only covers the growth of existing voids. The void nucleation phenomena should be incorporated into the framework.
- Although stress triaxiality is of high importance for void growth, the Lode parameter is also proven to be effective. The effect can be included in the framework by adding an L dependent growth term to the void evolution rule similar to the shear modified GTN model. In addition, the performance of a L dependent model can be tested through the presented RVE analysis at different constant L values.

- Fracture simulations with the presented framework showed similar behavior to the existing models. However, the model should also be validated with experimental studies under different boundary conditions. Moreover, the random void distribution in the real material can be simulated through the developed user material subroutine by using a position dependent random initial porosity.
- The presented model can be coupled with a recently developed porosity based cohesive zone model [94–97] to simulate crack initiation and propagation with physically consistent models.

REFERENCES

[1] A. C. F. Cocks, "Inelastic deformation of porous materials," *Journal of the Mechanics and Physics of Solids*, vol. 37, no. 6, pp. 693 – 715, 1989.

[2] H. C. Rogers, "The tensile fracture of ductile metals," *Transactions of the Metallurgical Society of AIME*, vol. 218, pp. 498–506, 1960.

[3] F. A. McClintock, "A Criterion for Ductile Fracture by the Growth of Holes," *Journal of Applied Mechanics*, vol. 35, no. 2, pp. 363–371, 1968.

[4] J. R. Rice and D. M. Tracey, "On the ductile enlargement of voids in triaxial stress fields," *Journal of the Mechanics and Physics of Solids*, vol. 17, no. 3, pp. 201 – 217, 1969.

[5] A. S. Argon and J. Im, "Separation of second phase particles in spheroidized 1045 steel, cu-0.6pct cr alloy, and maraging steel in plastic straining," *Metallurgical Transactions A*, vol. 6, no. 4, p. 839, 1975.

[6] L. Babout, Y. Brechet, E. Maire, and R. Fougères, "On the competition between particle fracture and particle decohesion in metal matrix composites," *Acta Materialia*, vol. 52, no. 15, pp. 4517 – 4525, 2004.

[7] M. N. Shabrov, C. L. Briant, A. Needleman, S. Kim, E. Sylven, D. H. Sherman, and L. Chuzhoy, "Void nucleation by inclusion cracking," *Metallurgical and Materials Transactions A*, vol. 35, no. 6, pp. 1745–1755, 2004.

[8] A. Weck, D. S. Wilkinson, and E. Maire, "Observation of void nucleation, growth and coalescence in a model metal matrix composite using x-ray tomography," *Materials Science and Engineering: A*, vol. 488, no. 1, pp. 435 – 445, 2008.

[9] A. Pineau, A. A. Benzerga, and T. Pardoen, "Failure of metals i: Brittle and ductile fracture," *Acta Materialia*, vol. 107, pp. 424 – 483, 2016.

[10] M. Achouri, G. Germain, P. Dal Santo, and D. Saidane, "Experimental characterization and numerical modeling of micromechanical damage under different stress states," *Materials & Design*, vol. 50, pp. 207 – 222, 2013.

[11] N. Kanetake, M. Nomura, and T. Choh, "Continuous observation of microstructural degradation during tensile loading of particle reinforced aluminium matrix composites," *Materials Science and Technology*, vol. 11, no. 12, pp. 1246–1252, 1995.

[12] A. Weck and D. S. Wilkinson, "Experimental investigation of void coalescence in metallic sheets containing laser drilled holes," *Acta Materialia*, vol. 56, no. 8, pp. 1774 – 1784, 2008.

[13] J. W. Hancock and A. C. Mackenzie, "On the mechanisms of ductile failure in high-strength steels subjected to multi-axial stress-states," *Journal of the Mechanics and Physics of Solids*, vol. 24, no. 2, pp. 147 – 160, 1976.

[14] A. C. Mackenzie, J. W. Hancock, and D. K. Brown, "On the influence of state of stress on ductile failure initiation in high strength steels," *Engineering Fracture Mechanics*, vol. 9, no. 1, pp. 167 – 188, 1977.

[15] J. W. Hancock and D. K. Brown, "On the role of strain and stress state in ductile failure," *Journal of the Mechanics and Physics of Solids*, vol. 31, no. 1, pp. 1 – 24, 1983.

[16] R. Becker, A. Needleman, O. Richmond, and V. Tvergaard, "Void growth and failure in notched bars," *Journal of the Mechanics and Physics of Solids*, vol. 36, no. 3, pp. 317 – 351, 1988.

[17] K. Decamp, L. Bauvineau, J. Besson, and A. Pineau, "Size and geometry effects on ductile rupture of notched bars in a c-mn steel: experiments and modelling," *International Journal of Fracture*, vol. 88, no. 1, pp. 1–18, 1997.

[18] Y. Bao and T. Wierzbicki, "On fracture locus in the equivalent strain and stress triaxiality space," *International Journal of Mechanical Sciences*, vol. 46, no. 1, pp. 81 – 98, 2004.

[19] T. B. Cox and J. R. Low, "An investigation of the plastic fracture of aisi 4340 and 18 nickel-200 grade maraging steels," *Metallurgical Transactions*, vol. 5, no. 6, pp. 1457–1470, 1974.

[20] I. Barsoum and J. Faleskog, "Rupture mechanisms in combined tension and shear—Experiments," *International Journal of Solids and Structures*, vol. 44, no. 6, pp. 1768 – 1786, 2007.

[21] C. Tekoğlu, J. W. Hutchinson, and T. Pardoen, "On localization and void coalescence as a precursor to ductile fracture," *Philosophical Transactions of the Royal Society A: Mathematical, Physical and Engineering Sciences*, vol. 373, no. 2038, p. 20140121, 2015.

[22] L. M. Kachanov, "Rupture time under creep conditions," 1958.

[23] J.-L. Chaboche, "Continuous damage mechanics — a tool to describe phenomena before crack initiation," *Nuclear Engineering and Design*, vol. 64, no. 2, pp. 233 – 247, 1981.

[24] P. Areias, N. Van Goethem, and E. B. Pires, "A damage model for ductile crack initiation and propagation," *Computational Mechanics*, vol. 47, no. 6, pp. 641–656, 2011.

[25] G. R. Johnson and W. H. Cook, "Fracture characteristics of three metals subjected to various strains, strain rates, temperatures and pressures," *Engineering Fracture Mechanics*, vol. 21, no. 1, pp. 31 – 48, 1985.

[26] Y. Bai and T. Wierzbicki, "Application of extended mohr–coulomb criterion to ductile fracture," *International Journal of Fracture*, vol. 161, no. 1, p. 1, 2010.

[27] D. Mohr and S. J. Marcadet, "Micromechanically-motivated phenomenological hosford–coulomb model for predicting ductile fracture initiation at low stress triaxialities," *International Journal of Solids and Structures*, vol. 67-68, pp. 40 – 55, 2015.

[28] Y. Li, M. Luo, J. Gerlach, and T. Wierzbicki, "Prediction of shear-induced fracture in sheet metal forming," *Journal of Materials Processing Technology*, vol. 210, no. 14, pp. 1858 – 1869, 2010.

[29] Y. Lou, H. Huh, S. Lim, and K. Pack, "New ductile fracture criterion for prediction of fracture forming limit diagrams of sheet metals," *International Journal of Solids and Structures*, vol. 49, no. 25, pp. 3605 – 3615, 2012.

[30] Y. Huang, "Accurate Dilatation Rates for Spherical Voids in Triaxial Stress Fields," *Journal of Applied Mechanics*, vol. 58, no. 4, pp. 1084–1086, 1991.

[31] G. Rousselier, "Ductile fracture models and their potential in local approach of fracture," *Nuclear Engineering and Design*, vol. 105, no. 1, pp. 97 – 111, 1987.

[32] J. Lemaitre, "A Continuous Damage Mechanics Model for Ductile Fracture," *Journal of Engineering Materials and Technology*, vol. 107, no. 1, pp. 83–89, 1985.

[33] B. Tanguy and J. Besson, "An extension of the rousselier model to viscoplastic temperature dependent materials," *International Journal of Fracture*, vol. 116, pp. 81–101, 2002.

[34] A. L. Gurson, "Continuum Theory of Ductile Rupture by Void Nucleation and Growth: Part I—Yield Criteria and Flow Rules for Porous Ductile Media," *Journal of Engineering Materials and Technology*, vol. 99, no. 1, pp. 2–15, 1977.

[35] C. C. Chu and A. Needleman, "Void Nucleation Effects in Biaxially Stretched Sheets," *Journal of Engineering Materials and Technology*, vol. 102, no. 3, pp. 249–256, 1980.

[36] V. Tvergaard, "Influence of voids on shear band instabilities under plane strain conditions," *International Journal of Fracture*, vol. 17, no. 4, pp. 389–407, 1981.

[37] V. Tvergaard, "On localization in ductile materials containing spherical voids," *International Journal of Fracture*, vol. 18, no. 4, pp. 237–252, 1982.

[38] J. Koplik and A. Needleman, "Void growth and coalescence in porous plastic solids," *International Journal of Solids and Structures*, vol. 24, no. 8, pp. 835 – 853, 1988.

[39] G. Perrin and J.-B. Leblond, "Analytical study of a hollow sphere made of plastic porous material and subjected to hydrostatic tension-application to some

problems in ductile fracture of metals," *International Journal of Plasticity*, vol. 6, no. 6, pp. 677 – 699, 1990.

[40] J. Faleskog, X. Gao, and C. F. Shih, "Cell model for nonlinear fracture analysis – i. micromechanics calibration," *International Journal of Fracture*, vol. 89, no. 4, pp. 355–373, 1998.

[41] V. Tvergaard and A. Needleman, "Analysis of the cup-cone fracture in a round tensile bar," *Acta Metallurgica*, vol. 32, no. 1, pp. 157 – 169, 1984.

[42] M. Gologanu, J.-B. Leblond, and J. Devaux, "Approximate models for ductile metals containing non-spherical voids—case of axisymmetric prolate ellipsoidal cavities," *Journal of the Mechanics and Physics of Solids*, vol. 41, no. 11, pp. 1723 – 1754, 1993.

[43] M. Gologanu, J.-B. Leblond, and J. Devaux, "Approximate models for ductile metals containing nonspherical voids—case of axisymmetric oblate ellipsoidal cavities," *Journal of Engineering Materials and Technology*, vol. 116, no. 3, pp. 290–297, 1994.

[44] M. Gologanu, J.-B. Leblond, G. Perrin, and J. Devaux, *Recent Extensions of Gurson's Model for Porous Ductile Metals*, pp. 61–130. Vienna: Springer Vienna, 1997.

[45] L. Xue, "Constitutive modeling of void shearing effect in ductile fracture of porous materials," *Engineering Fracture Mechanics*, vol. 75, no. 11, pp. 3343 – 3366, 2008.

[46] K. Nahshon and J. W. Hutchinson, "Modification of the gurson model for shear failure," *European Journal of Mechanics - A/Solids*, vol. 27, no. 1, pp. 1 – 17, 2008.

[47] L. E. Dæhli, D. Morin, T. Børvik, and O. S. Hopperstad, "A lode-dependent gurson model motivated by unit cell analyses," *Engineering Fracture Mechanics*, vol. 190, pp. 299 – 318, 2018.

[48] K. L. Nielsen and V. Tvergaard, "Effect of a shear modified gurson model on damage development in a fsw tensile specimen," *International Journal of Solids and Structures*, vol. 46, no. 3, pp. 587 – 601, 2009.

[49] M. Dunand and D. Mohr, "On the predictive capabilities of the shear modified gurson and the modified mohr–coulomb fracture models over a wide range of stress triaxialities and lode angles," *Journal of the Mechanics and Physics of Solids*, vol. 59, no. 7, pp. 1374 – 1394, 2011.

[50] A. A. Benzerga and J. Besson, "Plastic potentials for anisotropic porous solids," *European Journal of Mechanics - A/Solids*, vol. 20, no. 3, pp. 397 – 434, 2001.

[51] J. Wen, Y. Huang, K. C. Hwang, C. Liu, and M. Li, "The modified gurson model accounting for the void size effect," *International Journal of Plasticity*, vol. 21, no. 2, pp. 381 – 395, 2005.

[52] V. Monchiet and G. Bonnet, "A gurson-type model accounting for void size effects," *International Journal of Solids and Structures*, vol. 50, no. 2, pp. 320 – 327, 2013.

[53] L. Morin, D. Kondo, and J.-B. Leblond, "Numerical assessment, implementation and application of an extended gurson model accounting for void size effects," *European Journal of Mechanics - A/Solids*, vol. 51, pp. 183 – 192, 2015.

[54] H. Yu, J. S. Olsen, A. Alvaro, L. Qiao, J. He, and Z. Zhang, "Hydrogen informed gurson model for hydrogen embrittlement simulation," *Engineering Fracture Mechanics*, vol. 217, p. 106542, 2019.

[55] S. Bergo, D. Morin, T. Børvik, and O. S. Hopperstad, "Micromechanics-based identification of a ductile fracture model for three structural steels," *Engineering Fracture Mechanics*, vol. 224, p. 106803, 2020.

[56] P. Ponte Castañeda, "The effective mechanical properties of nonlinear isotropic composites," *Journal of the Mechanics and Physics of Solids*, vol. 39, no. 1, pp. 45 – 71, 1991.

[57] P. Sofronis and R. M. McMeeking, "Creep of Power-Law Material Containing Spherical Voids," *Journal of Applied Mechanics*, vol. 59, no. 2S, pp. S88–S95, 1992.

[58] J. Besson and A. G. Evans, "The effect of reinforcements on the densification of a metal powder," *Acta Metallurgica et Materialia*, vol. 40, no. 9, pp. 2247 – 2255, 1992.

[59] J. M. Duva and P. D. Crow, "The densification of powders by power-law creep during hot isostatic pressing," *Acta Metallurgica et Materialia*, vol. 40, no. 1, pp. 31 – 35, 1992.

[60] J. M. Duva and P. D. Crow, "Analysis of consolidation of reinforced materials by power-law creep," *Mechanics of Materials*, vol. 17, no. 1, pp. 25 – 32, 1994.

[61] A. Needleman, "Void Growth in an Elastic-Plastic Medium," *Journal of Applied Mechanics*, vol. 39, no. 4, pp. 964–970, 1972.

[62] J. Kim, X. Gao, and T. S. Srivatsan, "Modeling of void growth in ductile solids: effects of stress triaxiality and initial porosity," *Engineering Fracture Mechanics*, vol. 71, no. 3, pp. 379 – 400, 2004.

[63] T. Pardoen and J. W. Hutchinson, "An extended model for void growth and coalescence," *Journal of the Mechanics and Physics of Solids*, vol. 48, no. 12, pp. 2467 – 2512, 2000.

[64] I. Barsoum and J. Faleskog, "Rupture mechanisms in combined tension and shear—Micromechanics," *International Journal of Solids and Structures*, vol. 44, no. 17, pp. 5481 – 5498, 2007.

[65] M. Dunand and D. Mohr, "Effect of lode parameter on plastic flow localization after proportional loading at low stress triaxialities," *Journal of the Mechanics and Physics of Solids*, vol. 66, pp. 133 – 153, 2014.

[66] S. K. Yerra, C. Tekoğlu, F. Scheyvaerts, L. Delannay, P. Van Houtte, and T. Pardoen, "Void growth and coalescence in single crystals," *International Journal of Solids and Structures*, vol. 47, no. 7, pp. 1016 – 1029, 2010.

[67] U. B. Asim, M. A. Siddiq, and M. E. Kartal, "Representative volume element (rve) based crystal plasticity study of void growth on phase boundary in titanium alloys," *Computational Materials Science*, vol. 161, pp. 346 – 350, 2019.

[68] H.-J. Guo, C. Ling, E. P. Busso, Z. Zhong, and D.-F. Li, "Crystal plasticity based investigation of micro-void evolution under multi-axial loading conditions," *International Journal of Plasticity*, vol. 129, p. 102673, 2020.

[69] R. D. Thomson and J. W. Hancock, "Local stress and strain fields near a spherical elastic inclusion in a plastically deforming matrix," *International Journal of Fracture*, vol. 24, no. 3, pp. 209–228, 1984.

[70] L. Babout, E. Maire, and R. Fougères, "Damage initiation in model metallic materials: X-ray tomography and modelling," *Acta Materialia*, vol. 52, no. 8, pp. 2475 – 2487, 2004.

[71] A. Needleman, "A Continuum Model for Void Nucleation by Inclusion Debonding," *Journal of Applied Mechanics*, vol. 54, no. 3, pp. 525–531, 1987.

[72] M. N. Shabrov and A. Needleman, "An analysis of inclusion morphology effects on void nucleation," *Modelling and Simulation in Materials Science and Engineering*, vol. 10, no. 2, pp. 163–183, 2002.

[73] T. Yalçınkaya, C. Erdoğan, İ. T. Tandogan, and A. Cocks, "Formulation and implementation of a new porous plasticity model," *Procedia Structural Integrity*, vol. 21, pp. 46 – 51, 2019.

[74] ABAQUS, "The Abaqus documentation collection, version 6.14.," *Dassault Systèmes, Providence, Rhode Island*, 2014.

[75] J. C. Simo and R. L. Taylor, "Consistent tangent operators for rate-independent elastoplasticity," *Computer Methods in Applied Mechanics and Engineering*, vol. 48, no. 1, pp. 101 – 118, 1985.

[76] R. C. Lin, D. Steglich, W. Brocks, and J. Betten, "Performing rve calculations under constant stress triaxiality for monotonous and cyclic loading," *International Journal for Numerical Methods in Engineering*, vol. 66, no. 8, pp. 1331–1360, 2006.

[77] C. Tekoğlu, "Representative volume element calculations under constant stress triaxiality, lode parameter, and shear ratio," *International Journal of Solids and Structures*, vol. 51, no. 25, pp. 4544 – 4553, 2014.

[78] T. Yalçınkaya, G. Ö. Güngör, S. O. Çakmak, and C. Tekoğlu, "A micromechanics based numerical investigation of dual phase steels," *Procedia Structural Integrity*, vol. 21, pp. 61 – 72, 2019.

[79] T. Yalçınkaya, S. O. Çakmak, and C. Tekoğlu, "A crystal plasticity based finite element framework for rve calculations of two-phase materials: Void nucleation in dual-phase steels," *Finite Elements in Analysis and Design*, vol. 187, p. 103510, 2021.

[80] G. Ö. Güngör, "Microstructural modelling of dual-phase steels through polycrystalline plasticity at rve level," Master's thesis, Middle East Technical University, 2020.

[81] A. A. Benzerga and J.-B. Leblond, "Ductile fracture by void growth to coalescence," in *Advances in Applied Mechanics* (H. Aref and E. van der Giessen, eds.), vol. 44 of *Advances in Applied Mechanics*, pp. 169 – 305, Elsevier, 2010.

[82] Z.-P. Wang, K. Y. Lam, and B. Cotterell, "An approximate yield criterion for voided nonlinear materials," *Mechanics of Materials*, vol. 22, no. 4, pp. 291 – 300, 1996.

[83] B. Budiansky, J. W. Hutchinson, and S. Slutsky, "Void growth and collapse in viscous solids," in *Mechanics of Solids* (H. G. HOPKINS and M. J. SEWELL, eds.), pp. 13 – 45, Oxford: Pergamon, 1982.

[84] N. Aravas, "On the numerical integration of a class of pressure-dependent plasticity models," *International Journal for Numerical Methods in Engineering*, vol. 24, no. 7, pp. 1395–1416, 1987.

[85] F. Scheyvaerts, T. Pardoen, and P. R. Onck, "A new model for void coalescence by internal necking," *International Journal of Damage Mechanics*, vol. 19, no. 1, pp. 95–126, 2010.

[86] C. Tekoğlu, J.-B. Leblond, and T. Pardoen, "A criterion for the onset of void coalescence under combined tension and shear," *Journal of the Mechanics and Physics of Solids*, vol. 60, no. 7, pp. 1363 – 1381, 2012.

[87] S. M. Keralavarma and S. Chockalingam, "A criterion for void coalescence in anisotropic ductile materials," *International Journal of Plasticity*, vol. 82, pp. 159 – 176, 2016.

[88] M. E. Torki, "A unified criterion for void growth and coalescence under combined tension and shear," *International Journal of Plasticity*, vol. 119, pp. 57 – 84, 2019.

[89] A. Needleman and V. Tvergaard, "An analysis of ductile rupture in notched bars," *Journal of the Mechanics and Physics of Solids*, vol. 32, no. 6, pp. 461 – 490, 1984.

[90] T. Wierzbicki, Y. Bao, Y.-W. Lee, and Y. Bai, "Calibration and evaluation of seven fracture models," *International Journal of Mechanical Sciences*, vol. 47, no. 4-5 SPEC. ISS., pp. 719–743, 2005.

[91] H. Li, M. W. Fu, J. Lu, and H. Yang, "Ductile fracture: Experiments and computations," *International Journal of Plasticity*, vol. 27, no. 2, pp. 147 – 180, 2011.

[92] M. Asano, M. Yuasa, H. Miyamoto, T. Tanaka, C. Erdoğan, and T. Yalçınkaya, "Potential of high compressive ductility of ultrafine grained copper fabricated by severe plastic deformation," *Metals*, vol. 10, no. 11, 2020.

[93] J. Besson, D. Steglich, and W. Brocks, "Modeling of crack growth in round bars and plane strain specimens," *International Journal of Solids and Structures*, vol. 38, no. 46, pp. 8259 – 8284, 2001.

[94] T. Yalçınkaya and A. Cocks, "Physics based formulation of a cohesive zone model for ductile fracture," *Key Engineering Materials*, vol. 651-653, p. 993, 2015.

[95] T. Yalçınkaya and A. Cocks, "Micromechanical cohesive zone relations for ductile fracture," *Procedia Structural Integrity*, vol. 2, pp. 1716 – 1723, 2016.

[96] T. Yalçınkaya, İ. T. Tandoğan, and A. Cocks, "Development of a micromechanics based cohesive zone model and application for ductile fracture," *Procedia Structural Integrity*, vol. 21, pp. 52 – 60, 2019.

[97] İ. T. Tandoğan, "Ductile fracture of metallic materials through micromechanics based cohesive zone elements," Master's thesis, Middle East Technical University, 2020.